ELUCIDATING THE PHYSICAL STABILITY AND FORMATION MECHANISM OF AMORPHOUS PROBUCOL NANOPARTICLE FORMED BY AQUEOUS DISPERSION OF TERNARY SOLID DISPERSION

ZHIJING ZHAO

A DISSERTATION SUBMITTED IN PARTIAL FULFILMENT OF

THE REQUIREMENT FOR THE DEGREE OF

DOCTOR OF PHILOSOPHY

(PHARMACEUTICAL SCIENCES)

LABORATORY OF PHARMACEUTICAL TECHNOLOGY

GRADUATE SCHOOL OF PHARMACEUTICAL SCIENCES

CHIBA UNIVERSITY

JAPAN

2021

CONTENTS

ABSTRACT ..... **- 3 -**

INTRODUCTION ..... **- 6 -**

EXPERIMENTAL ..... **- 12 -**

PART I. IMPACT OF PREPARATION METHODS OF TERNARY SOLID DISPERSIONS ON THE PHYSICAL STABILITY OF PBC AMORPHOUS DRUG NANOPARTICLES ..... - 14 -

PART II. IMPACT OF COMPOSITION OF TERNARY SOLID DISPERSIONS ON THE FORMATION OF PBC AMORPHOUS DRUG NANOPARTICLES ..... - 20 -

RESULT AND DISCUSSION ..... **- 24 -**

PART I. IMPACT OF PREPARATION METHODS OF TERNARY SOLID DISPERSIONS ON THE PHYSICAL STABILITY OF PBC AMORPHOUS DRUG NANOPARTICLES ..... - 24 -

Characterization of the spray-dried sample (SPD) and the ground mixtures (GMs)... - 24 -

Characterization of the SPD and GM suspensions ..... - 33 -

Discussion of nanoparticle evolution in aqueous solution. ..... - 53 -

PART II. IMPACT OF COMPOSITION OF TERNARY SOLID DISPERSIONS ON THE FORMATION OF PBC AMORPHOUS DRUG NANOPARTICLES ..... - 58 -

Characterization of the solid dispersions (SDs) ..... - 58 -

Characterization of the SD suspensions ..... - 64 -

Discussion of the effect of HPMC and SDS on the formation of amorphous PBC nanoparticles ..... - 77 -

CONCLUSIONS ..... **- 83 -**

FUTURE DIRECTIONS ..... **- 86 -**

ACKNOWLEDGEMENTS ..... **- 89 -**

REFERENCE ..... **- 91 -**

LIST OF PUBLICATIONS ..... **- 95 -**

THESIS COMMITTEE ..... **- 96 -**

ABSTRACT

The present study emphasized the formulation of the amorphous drug nanoparticle formed by aqueous dispersion of drug/polymer/surfactant ternary solid dispersion (SD). The relation between the molecular state of the drug in SDs and the stability and formation of formed amorphous drug nanoparticles was elucidated. The impact of different trace crystallinities depending on different preparation methods of ternary SD on the physical stability of amorphous drug nanoparticles formed after aqueous dispersion was investigated in Part I. The impact of composition−induced different miscibility between drug and polymer and phase-separated domain size in SDs on the morphological variation of amorphous drug nanoparticles was revealed in Part II. Besides, we detailly discussed the effect of the polymer, hypromellose (HPMC), and the surfactant, sodium dodecyl sulfate (SDS), on the formation of amorphous drug nanoparticles during water immersion in SDs and after aqueous dispersion.

In Part I, spray drying and co-grinding were used to prepare a spray-dried sample (SPD) and two ground mixtures (GM (I) and GM (II)) of probucol (PBC) form I and form II/HPMC/SDS ternary SDs, respectively. The amorphization of PBC in the SPDs and GMs was confirmed using powder X-ray diffraction (PXRD) and solid-state ^{13}C nuclear magnetic resonance (NMR) spectroscopy. However, differential scanning calorimetry showed that small amounts of PBC nucleus or PBC-rich domains remained in both GMs. Then, the nanoparticles were formed by dispersing ternary SDs of PBC in water. The time-dependent evolution of amorphous PBC nanoparticles was characterized by cryogenic transmission electron microscopy (cryo-TEM) and atomic force microscopy (AFM). The physical stability of drug nanoparticles formed after

aqueous dispersion in the SPD and GM suspensions during storage at 40 °C was characterized. Cryo-TEM showed that the spherical nanoparticles smaller than 30 nm were observed in all suspensions just after dispersion. The sizes of the particles in the SPD suspension gradually increased but remained on the order of nanometers and retained their spherical shape during storage. In contrast, both GM suspensions evolved through three morphologies, spherical nanoparticles that gradually increased in size, needle-like nanocrystals, and micrometer-sized crystals with various shapes. The evolution of the nanoparticles suggested that their stability in the GM suspension was lower than in the SPD suspension. PXRD analysis of the freeze-dried suspensions of the particles showed that the PBC in the nanoparticles of the SPD suspension was in the amorphous state just after dispersion. In contrast, a small fraction of the PBC in the nanoparticles of the GM suspension exhibited a crystal phase and selectively crystallized to its initial crystal form during storage. AFM force−distance curves also demonstrated the existence of crystal phase PBC in the spherical nanoparticles in the GM suspension just after dispersion. The molecular state of PBC in the ternary SD was dependent on the preparation methods (either completely amorphized or incompletely amorphized with residual nuclei or drug-rich domains) and determined the potential mechanisms of PBC nanoparticle evolution after aqueous dispersion. These findings confirm the importance of the molecular state on the particle evolution and the physical stability of the drug nanoparticles in the suspension.

In Part II, PBC/HPMC/SDS ternary SDs of different weight ratios were prepared and evaluated to unveil the effect of HPMC and SDS on the formation of amorphous PBC nanoparticles. The morphological variation of the PBC nanoparticles prepared using SDs of different compositions was determined using dynamic light scattering and cryo-TEM measurements. Statistical analysis

of particle size versus roundness was carried out using cryo-TEM images. An evident correlation was observed between the morphology of the PBC nanoparticles and the amount of HPMC and SDS, either admixed in SDs or pre-dissolved in an aqueous solution. The admixed HPMC in SDs was demonstrated to play a crucial role in determining the primary particle size of discrete amorphous PBC nanoparticles. Based on solid-state ^{13}C NMR spectroscopy, this phenomenon should be due to the enlarged size of the PBC-rich domain in SDs, which is dependent on the decreasing amounts of admixed HPMC. Although the pre-dissolved HPMC had less impact on the primary particle size, it inhibited the particle agglomeration and recrystallization of amorphous PBC nanoparticles. On the other hand, sufficient admixed SDS suppressed the size enhancement of the PBC-rich domains during water immersion and nanoparticle evolution (agglomeration and crystallization) after aqueous dispersion. The pre-dissolved SDS could restrain the agglomeration of amorphous PBC nanoparticles, ultimately forming hundreds of irregular nanometer-order structures. However, their sizes were still slightly larger than those obtained with a high portion of admixed SDS; this is because of the increase in size during water immersion. The findings of this study clarified the usefulness and necessity of adding polymers and surfactants to SDs to fabricate drug nanoparticle formulations effectively.

INTRODUCTION

In the last couple of decades, numerous amounts of novel pharmaceutically active molecules, which could potentially fulfill unmet medical needs, were discovered. Unfortunately, the discovered candidates are biased toward hydrophobic and crystalline, leading to poor aqueous solubility and low bioavailability. Up to 2010, 40% of approved drugs and 90% of developmental compounds were estimated to have low water solubility.[1-3] Currently, drug discovery even faces the difficulty of identifying drug candidates with an aqueous solubility above 10 μg/mL.[4] Several approaches have been utilized to increase the dissolution rate and solubility and thus oral bioavailability of poorly soluble drugs. Traditional approaches for improving drug dissolution rate and solubility include salt/polymorph formation[5, 6], solubilizing excipients[7], and complexation agents[8-10]. However, the successful formulation through these traditional approaches has been limited due to the arduous selection of highly soluble salts, as well as the requirement for large quantities of solubilizing excipients and complexation agents.

In recent years, solid dispersion (SD), a solid-solid blend of the amorphous state of an active pharmaceutical ingredient with a polymer excipient, has gained widespread attention to address the issue of low bioavailability of poorly water-soluble drugs. The amorphous state lacking the long-range order of molecular arrangement represents the most energetic solid-state of a material.[11, 12] The addition of polymer, which has complex structures, inhibits the recrystallization trend of the amorphous drug by hindering the molecular mobility and lowering the chemical potential.[11] Therefore, the high Gibbs free energy of amorphous drug and crystallizing inhibitive effect of polymer in SD enables the generation of supersaturation after aqueous dispersion, which

offers an ideal path for improving the bioavailability of active compounds.

Furthermore, several research pieces reported a kind of exciting phenomenon that the aqueous dispersion of SDs enables the generation of amorphous drug nanoparticles. Purohit et al. reported the formation of amorphous drug nanoparticles via the dispersion of ritonavir/polyvinylpyrrolidone (PVP) SD.[13] Ricarte et al. reported the direct observation of amorphous spherical nanoparticles during the aqueous dissolution of spray-dried probucol (PBC)/hypromellose acetate succinate (HPMCAS) SDs using cryogenic transmission electron microscopy (cryo-TEM).[14] The formation of amorphous drug nanoparticles by aqueous dispersion of SD catches more eyes due to the combined benefit of enlarged specific surface area [15-17] and Gibbs free energy. According to the Noyes-Whitney equation, when particle size is reduced, the total effective surface area increases, and thereby, the dissolution rate is enhanced. The reduction of particle size could also reduce the diffusion layer thickness surrounding the drug particles and increase concentration gradient[18-20]. Besides, an enlarged specific surface area could improve the adhesion of drugs to the mucosa of the gastrointestinal tract.[21] The amorphous state of the drug in nanoparticles offers an absolute or synergistic effect in solubility and dissolution rates due to much higher Gibbs' free energy than the crystalline drug.[22] In the ideal case for absorption, amorphous dug nanoparticles could act as a "reservoir" and gradually release the free drug in the bulk aqueous phase keeping the supersaturation at a high level during drug diffusion through the biological membranes.[4] Multiple papers and current studies have proposed that these colloidal amorphous drug nanoparticles are essential for enhancing drug bioavailability. [23-26]

Up to date, though numerous researches efforts to better characterize the dissolution process of SDs, the major SD formulation challenge associated with amorphous drug nanoparticles is

understanding their formation mechanism and improving their physical stability both before and after aqueous dispersion. The formulation design of SD-based amorphous drug nanoparticles should consider both the states before and after aqueous dispersion at the same time.

For the SD, the ideal case should be the active compound molecules homogeneously dispersed in polymer excipient. However, many factors could affect the molecular state of the drug and the miscibility between drug and polymer in SD, leading to component demixings, such as preparation method[27], drug loading[28], storage condition[29, 30], and excipient species[31]. Hence, an SD should exhibit one of the following three states due to the miscibility between the drug and polymer: (1) drug molecules homogeneously dispersed within the polymer matrix, (2) phase-separated domains of amorphous drug and polymer formed in SD, or (3) trace crystallinity of the drug in the SD. From a conceptual point of view, SD with phase separation is known to be unstable, leading to adverse effects on supersaturation maintenance and amorphous drug nanoparticle formation. Interestingly, Li et al. recently found that colloidal amorphous nanoparticles observed after water dispersion of a phase-separated SD could have origins related to the release of drug-rich domains from the SD matrix.[32] Therefore, elucidating the relationship between the solid-state nanostructure and the resulting amorphous drug nanoparticle formation could help to discover acceptable thresholds for designing SD formulations.

On the other hand, the amorphous drug nanoparticles formed after aqueous dispersion of SD face their own stability issue. The enlarged specific surface area of drug nanoparticles induces their agglomeration/aggregation for lowing the high surface tension. The enhanced Gibbs free energy forces the amorphous state of drug transfer into a more stable state, crystalline form. To stabilize amorphous drug nanoparticles in an aqueous solution, the addition of stabilizers, such as

polymers and surfactants, have been taken into account.[33] Hydrophilic polymers, such as PVP[34] and hypromellose (HPMC),[35, 36] and ionic surfactants, such as sodium dodecyl sulfate (SDS),[37] are effective in enhancing the water-dispersibility of drug nanoparticles by steric repulsion and electrostatic repulsion,[38] respectively. Besides, polymers can inhibit the recrystallization of drugs in amorphous nanoparticles and slow the crystal growth rate.[39] Therefore, understanding the effect of admixed excipients in SD on the particle evolution of amorphous drug nanoparticles after aqueous dispersion is another urgent need.

The previous research reported that the PBC/HPMC/SDS ternary SD could provide the amorphous drug nanoparticles with a mean volume diameter (MV) of 25 nm just after aqueous dispersion. This ternary mixture was selected as the model system for this study. PBC is a powerful anti-cholesteric drug with antioxidant and anti-inflammatory properties. However, its solubility in water at 25°C is only 5 ng/mL, severely restricting its administration development. HPMC, a widely utilized hydrophilic polymer, was selected as the polymer matrix for the preparation of SDs due to its inhibitive effect on nucleation and crystal growth.[11, 40] SDS, an ionic surfactant, could sufficiently enhance the water-dispersibility of drug nanoparticles by steric repulsion and electrostatic repulsion.[38 38]

In this study, two practical impacts, I) the preparation methods and II) the composition of ternary SDs, on the stability and formation of amorphous drug nanoparticles formed after aqueous dispersion, were discussed. In part I, PBC/HPMC/SDS ternary SDs were prepared by spray-drying and co-grinding, respectively. The impact of the different molecular states of PBC depending on the manufacturing methods of amorphous SD on the stability of amorphous PBC nanoparticles was investigated. For the co-grinding method, two polymorphs of PBC, stable form I and

metastable form II, were used as starring materials. The solid states of prepared ternary blends were characterized by powder X-ray diffraction (PXRD), solid-state ^{13}C nuclear magnetic resonance (NMR) measurement, differential scanning calorimetry analysis, and variable-temperature PXRD measurement. The particle evolution in each suspension on storage was intuitively monitored by dynamic light scattering (DLS), quantitative determination of particle size fraction, and cryo-TEM measurement. PXRD measurements characterized the change in the crystallinity of PBC in the nanoparticles during storage after freeze-drying. In addition, the mechanical properties of the nanoparticles in the freshly prepared SPD and GM suspensions were determined using atomic force microscopy (AFM) force−distance curves. The micrometer-sized particles observed in the GM suspensions after long-term storage were characterized using TEM and PXRD measurements. Finally, the correlation between the molecular state of PBC before and after aqueous dispersion and the potential stability mechanism of the amorphous drug nanoparticles were discussed.

In part II, the impact of the composition of polymer and surfactant on the nanostructure of ternary SDs and subsequent formation of amorphous drug nanoparticles was evaluated. Ternary SDs with various weight ratios of PBC/HPMC/SDS were prepared using the spray drying method. The crystallinity and molecular states of the ternary SDs depending on the various HPMC and SDS contents were characterized by PXRD and solid-state ^{13}C NMR measurements. The ternary SDs were then dispersed in the aqueous solution (distilled water or pre-dissolved HPMC/SDS solutions) to prepare the SD suspensions. Following aqueous dispersion, DLS analysis and cryo-TEM imaging were employed for evaluating the particle size and morphology of the PBC particles in the aqueous solution. Then, the scatter plotting of particle size (diameter) against the

roundness of selected amorphous PBC particles in each suspension was conducted to statically analyze the effect of HPMC and SDS on particle size enhancement and particle evolution. Finally, the molecular states of the PBC particles in suspensions were evaluated by PXRD measurement after freeze-drying. Finally, the impact of HPMC and SDS on solid-state SD samples, phase behavior of SD structure during immersion into the aqueous solution, and particle evolution/crystallization of amorphous PBC nanoparticles released from disintegrated SD were discussed.

EXPERIMENTAL

Materials.

Two probucol (PBC) polymorphs, the stable form I and metastable form II,[41] were utilized as the models of poorly water-soluble drugs. PBC (form I) was kindly gifted from Daiichi-Sankyo Co., Ltd. (Tokyo, Japan). PBC (form II) was prepared from PBC (form I). PBC (form I) was dissolved in dichloromethane/methanol = 1:1 (v/v) at a concentration of 5% (w/v). The solution was spray-dried using an ADL311S-A (Yamato Scientific Co., Ltd., Tokyo, Japan) under the following conditions to prepare PBC (form II), an inlet temperature of 65 °C, atomizing pressure of 0.05 MPa, and a solution feed rate of 4 g/mL. In PBC (form II), the C-S-C-S-C chain is extended, and the molecule exists as an asymmetrical structure. Conversely, this symmetry is lost in PBC (form I). Hypromellose (HPMC) (Type TC-5E, Mw ≈ 12 600) was gifted from Shin-Etsu Chemical Co., Ltd. (Tokyo, Japan). Sodium dodecyl sulfate (SDS) was purchased from Wako Pure Chemical Industries, Ltd. (Osaka, Japan). The chemical structures of the materials are shown in Figure 1.

(a)

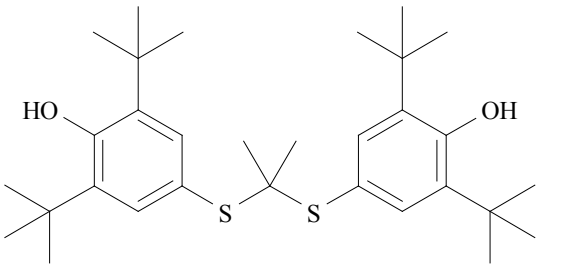

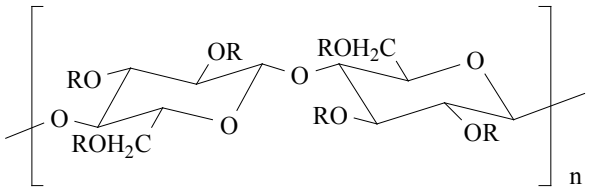

R= H, CH_3, $CH_2CH(CH_3)OH$

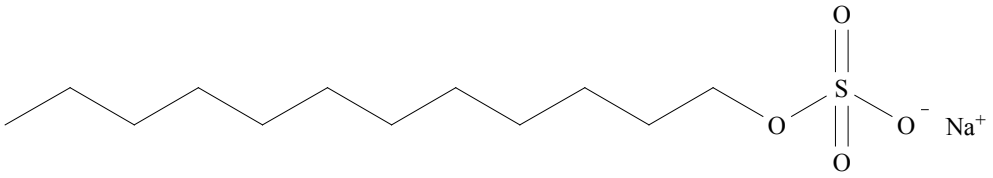

Figure 1. Chemical structures of (a) PBC, (b) HPMC, and (c) SDS. Carbon numbering for the nuclear magnetic resonance peak assignment is indicated in the figure.

PART I. IMPACT OF PREPARATION METHODS OF TERNARY SOLID DISPERSIONS ON THE PHYSICAL STABILITY OF PBC AMORPHOUS DRUG NANOPARTICLES

Sample Preparation Methods.

Preparation of the spray-dried sample (SPD). PBC, HPMC, and SDS were mixed at a weight ratio of 1:4:2 to obtain a physical mixture (PM). The PM was dissolved in dichloromethane/methanol = 1:1 (v/v) at a concentration of 5% (w/v). The solution was spray-dried using an ADL311S-A (Yamato Scientific Co., Ltd., Tokyo, Japan) under the following conditions to prepare the SPD, inlet temperature of 65 °C, atomizing pressure of 0.05 MPa, and a solution feed rate of 4 g/mL.

Preparation of the ground mixtures (GMs). PM(I) or (II), which was prepared using PBC (form I) or PBC (form II), was placed into a grinding cell and dipped in liquid nitrogen for 3 min for precooling. The PM was then ground in a vibrational rod mill (TI-200, CMT Co., Ltd., Fukushima, Japan) for 20 min. The cooling and grinding processes were repeated nine times to prepare the GM (I) and GM (II).

Preparation of the suspensions. Thirty-five milligrams of the SPD, GM (I), and GM (II) powder were dispersed in 10 mL of distilled water in 20 mL of glass vials at a PBC concentration of 0.5 mg/mL and then sonicated at a frequency of 42 kHz for 3 min to obtain SPD, GM (I), and GM (II) suspensions, respectively, using a Bransonic ultrasonic bath (B1510J-DTH, Yamato Scientific Co., Ltd., Tokyo, Japan). Each suspension was sealed with a parafilm and stored at 40 °C for 0, 1, 4, 8, and 12 days before characterization.

Preparation of the freeze-dried samples (FDs). The SPD and GM suspensions were freeze-dried after storage at 40 °C for 0, 1, 4, 8, and 12 days using a DRC-1100 freeze-dryer (Tokyo Rikakikai Co., Ltd., Tokyo, Japan). The freeze-drying conditions were as follows, prior to freezing, −40 °C for 2 h; primary drying, −20 °C for 12 h; and secondary drying, 20 °C for 5 h.

Characterization of the solid-state SPD and GMs.

Powder X-ray diffraction (PXRD) measurements. PXRD measurements were performed using a D8 ADVANCE (Bruker AXS, Germany) under the following experimental conditions, target, Cu; filter, Ni; voltage, 40 kV; current, 40 mA; and scanning angle, 5−30°. For the variable-temperature PXRD measurements, the heating rate was 5 °C/min. The PXRD measurements were carried out at temperatures of 25, 100, and 110 °C.

Solid-state ^{13}C nuclear magnetic resonance (NMR) spectroscopy. Solid-state ^{13}C NMR measurements were performed using a JNM-ECX400 NMR spectrometer with a magnetic field of 9.39 T (JEOL Resonance Co., Ltd., Tokyo, Japan). A pulse sequence with cross-polarization, dipolar decoupling, and total suppression of the spinning sidebands (CP/DD/TOSS) was utilized under magic-angle spinning (MAS) conditions. The NMR measurement conditions were as follows, contact time, 5 ms; data points, 2048; relaxation delay, 1−2 s; spinning rate, 5 kHz; and decoupling method, two-pulse phase-modulation. All the NMR spectra were externally referenced by setting the methyl peak of hexamethylbenzene to 17.3 ppm.

DSC measurements. DSC measurements were performed using a DSC Q2000 (TA Instruments, New Castle, DE, USA). Dry nitrogen was used as the inert gas at a flow rate of 50 mL/ min, and the measurements were carried out at 25−185 °C at a heating rate of 2 °C/min. Tzero aluminum

pans were used for the measurements.

Characterization of the SPD and GM nanosuspensions.

Particle size distribution. The mean volume diameter (MV) of the particles in the suspensions was determined by dynamic light scattering (DLS) with a Microtrac UPA (MicrotracBEL Corp., Japan; measurement range, 0.0008−6.5 μm), employing a wavelength of 780 nm, a laser power of 3 mW, and a heterodyne detector. The detector signal was digitized, and the frequency power spectrum of the signal was recorded using fast Fourier transform digital signal processing. Measurements were made under the following conditions, reflected light intensity, 281.4 mV; measurement time, 60 s; and repeat count, 3 times. Approximately 450 μL of sample suspension was added into the DLS cell immediately after being taken out from a 40 °C incubator. The polydispersity index (PDI) was calculated using equations (1) and (2) as per MicrotracBEL Corp., Japan (ISO 22412:2008). X_{DLS} (μm) and $\Delta Q_{int,\,i}$ indicate the average hydrodynamic diameter and intensity-weighted amount of particles with size X_i arbitrary units, respectively.

$$\overline{x_{DLS}} = \frac{\sum_{i=1}^{N} \Delta Q_{\mathrm{int},i}}{\sum_{i=1}^{N} \frac{\Delta Q_{\mathrm{int},i}}{x_i}} \quad \cdots\cdots \quad (1)$$

$$\mathrm{PDI} = 2\overline{x_{DLS}}^{2} \frac{\sum_{i=1}^{N} \Delta Q_{\mathrm{int},i} \left(1/x_i^2 - 1/\overline{x_{DLS}}^{2} \right)}{\sum_{i=1}^{N} \Delta Q_{\mathrm{int},i}} \quad \cdots\cdots \quad (2)$$

Quantification of the nanoparticles (<0.45 μm). At each storage time point (0, 1, 4, 8, and 12 days), the suspensions (PBC concentration of 0.5 mg/mL) stored at 40 °C were filtered through a 0.45 μm filter (cellulose acetate disposable syringe filter, Millipore). Due to the extremely low

solubility of the PBC crystals and amorphous PBC, the dissolved PBC was negligible. The PBC concentration in the nanoparticle fraction that passed through a 0.45 μm filter was determined by high-performance liquid chromatography (HPLC). The filtrates were diluted with acetonitrile (1:1) and separated using an Inertsil ODS-2 column (150 × 4.6 mm, 5 μm) at 40 °C; the detection wavelength was 242 nm. The mobile phase for PBC was acetonitrile/water/trifluoroacetic acid = 90:10:0.1 (v/v), and the injection volume and flow rate were 10 μL and 1 mL/ min, respectively.

Cryogenic transmission electron microscopy (cryo-TEM) and TEM measurements. Cryo-TEM and TEM measurements were conducted with an accelerating voltage of 120 kV using a JEM-2100F field emission TEM apparatus (JEOL Co., Ltd., Japan). For cryo-TEM, 2 μL of a prepared suspension was deposited on a 200 mesh copper grid covered with holey carbon film (Nisshin EM Co., Ltd., Tokyo, Japan). A thin aqueous film (ca. 100 nm thick) of the nanoparticle suspension was prepared by blotting the excess liquid and was rapidly vitrified by immersion in liquid ethane using a Leica CPC cryo-preparation chamber (Leica Microsystems, Wetzlar, Germany). The grid with the vitrified thin film was set on a sample holder and transferred into the microscope chamber. The sample temperature was kept below −170 °C using liquid nitrogen. Images were recorded using a CCD camera. ImageJ software (National Institutes of Health, USA) was used to conduct a statistical analysis of the particle size in the cryo-TEM images. For the TEM measurements, imaging was conducted on powder samples. The GM (I) and GM (II) suspensions were centrifuged at 1000g for 20 min at 25 °C to obtain the precipitates. The precipitates were freeze-dried using a DRC-1100 freeze-dryer (Tokyo Rikakikai Co., Ltd. Tokyo, Japan). The freeze-drying conditions were as follows, prior to freezing, −40 °C for 2 h; pressure reduction, −40 °C for 2 h; primary drying, −20 °C for 5 h; and secondary drying, 20 °C for 3 h.

Each of the obtained freeze-dried powders was dispersed on a hydrophilic-treated TEM grid supported with a collodion film (Cu 200, Nisshin EM Co., Ltd., Tokyo, Japan), and the excess sample was removed.

Atomic force microscopy (AFM) measurements. An MFP-3D AFM apparatus (Oxford Instruments, Osaka, Japan) was used to evaluate the topography and stiffness of the nanoparticles in the aqueous solution. The cleaved mica surface was modified with (3-Aminopropyl) triethoxysilane (APTES) under vacuum for 1 h to create the positively charged mica (AP-mica) surface. The positively charged mica surface electrostatically immobilized the negatively charged drug nanoparticles. The sample suspension was dropped onto the positively charged AP-mica surface, incubated for 8 h at room temperature, and diluted 100-fold with distilled water. Height images and cross-sectional profiles of the nanoparticles adsorbed on the mica surface were recorded in the tapping mode.

The silicon cantilevers (BL-AC40TS-C2, Olympus Co., Ltd. Tokyo, Japan) with a 40 nm thick gold/chromium reflex coating were utilized. The cantilever spring constant was 0.09 N/m and was calibrated using thermal oscillation. The resonance frequency was 25 kHz in the solution environment. The tip was a tetrahedron with a typical curvature radius of 8 nm and an effective tip height of 3.5 μm; the tip was measured using imaging gratings. The 1024 × 128 pixel images were captured in height mode in a JPEG format. Subsequently, all images were flattened using Nanoscope software. The same software was used for cross-sectional analysis. The other AFM measurement conditions were as follows, scanning speed, 0.70 Hz; scanning scale, 1 μm × 1 μm; and temperature, 25 °C. After imaging the samples using the tapping mode, a series of force−distance investigations on the selected points on the nanoparticles were performed. For the

sake of obtaining a reference from a hard surface, the adjacent substrate regions were also investigated. The inverse optical lever sensitivity (InvOLS) was calibrated using 30 force−distance curves conducted on the hard surface using the force−distance curves measured with a trigger point in a force channel of 5 nN. The InvOLS was calculated in the range of deflection from 0.1 to 0.5 V, and its histogram was fitted to Gaussian distribution. The mean value of InvOLS was 85.02 nm/V. This value was used in the following experiment to convert the voltage (deflection (V)) detected by the photodetector into deflection (nm). Based on these conditions, the mechanical properties of 50 nanoparticles for each sample were evaluated using the force-distance curves measured with the same trigger point of 5 nN.

Quantitative evaluation of HPMC and SDS concentration in the liquid phase. Solution-state ^{1}H NMR measurements were performed using a JNM-ECA500 NMR spectrometer with a magnetic field of 11.74 T (JEOL Resonance Co., Ltd., Tokyo, Japan). NMR spectra were obtained under the following conditions, data points, 32768; relaxation delay, 5 s; scans, 64; and spinning rate, 15 Hz. Trimethylsilyl propionate (TSP) was used as an internal reference. Deuterium oxide containing 0.5% TSP was used as the solvent for preparing the SPD, GM (I), and GM (II) suspensions at a PBC concentration of 0.5 mg/mL. The calibration curves were constructed using an HPMC and SDS solution as a standard. The peak area ratio of the respective peaks in the low (2.9−4.2 ppm) and high (0.6−1.9 ppm) magnetic fields was plotted against the TSP peak. All of the calibration curves exhibited good linearity ($R^2 > 0.995$). The concentrations of HPMC and SDS were calculated by solving two simultaneous equations.

$$AUC_{(2.9\text{-}4.2\ ppm)} = AUC_{(2.9\text{-}4.2\ ppm)HPMC} + AUC_{(2.9\text{-}4.2\ ppm)SDS}$$

$$AUC_{(0.6\text{-}1,9\ ppm)} = AUC_{(0.6\text{-}1,9\ ppm)HPMC} + AUC_{(0.6\text{-}1,9\ ppm)SDS}$$

PART II. IMPACT OF COMPOSITION OF TERNARY SOLID DISPERSIONS ON THE FORMATION OF PBC AMORPHOUS DRUG NANOPARTICLES

Sample preparation methods

Preparation of the solid dispersions (SDs). PBC, HPMC, and SDS were mixed at a weight ratio of 1:X:Y (X = 0.3, 0.5, 1, 2, 4; Y = 0, 0.3, 0.5, 1, 2) to obtain a physical mixture (PM). The PMs were dissolved in dichloromethane/methanol 1:1 (v/v) at 25°C at a concentration of 5% (w/v). The absence of polymeric agglomeration was confirmed in all stock solutions using DLS. Thereafter, each solution was spray-dried using an ADL311S-A (Yamato Scientific Co., Ltd., Tokyo, Japan) system with an inlet temperature of 65 °C, atomizing pressure of 0.05 MPa, and solution feed rate of 4 g/mL to prepare the SDs. The SD samples prepared with a certain weight ratio of PBC/HPMC/SDS (1:X:Y) are abbreviated as SD (1:X:Y) throughout the text.

Preparation of the SD suspensions. Three protocols were used to prepare the SD suspensions. In protocol 1, each SD was directly dispersed in 5 mL of distilled water at a PBC concentration of 0.5 mg/mL. In protocol 2, different amounts of HPMC and SDS were dispersed in distilled water, in advance, according to the amount of HPMC and SDS in each SD. Accordingly, the total input amounts of PBC, HPMC, and SDS in the final suspension was equal to 0.5, 2.0, and 1.0 mg/mL (weight ratio of 1:4:2), respectively. Based on protocol 2, additional SDS was added to the HPMC/SDS solution in protocol 3. Therefore, the total input amounts of PBC, HPMC, and SDS in each final suspension were 0.5, 2.0, and 1.5 mg/mL (weight ratio of 1:4:3), respectively. After aqueous dispersion, each SD suspension was sonicated at a frequency of 42 kHz for 1 min using a Bransonic® ultrasonic bath (B1510J-DTH, Yamato Scientific Co., Ltd., Tokyo, Japan).

Preparation of the freeze-dried samples (FDs). The SD suspensions were freeze-dried using a DRC-1100 freeze dryer (Tokyo Rikakikai Co., Ltd. Tokyo, Japan). The freeze-drying conditions were: pre-freezing, –40 °C for 2 h; primary drying, –20 °C for 12 h; and secondary drying, 20 °C for 5 h.

Characterization of the ternary SDs

PXRD measurement. PXRD measurements were acquired with a D8 ADVANCE instrument (Bruker AXS, Germany), with the following experimental conditions: target, Cu; filter, Ni; voltage, 40 kV; current, 40 mA; and scanning angle, 5–30°.

Solid-state ^{13}C NMR spectroscopy. Solid-state ^{13}C NMR measurements were obtained on a JNM-ECX400 NMR spectrometer, with a magnetic field of 9.39 T (JEOL Resonance Co., Ltd. Tokyo, Japan). A pulse sequence with cross-polarization, magic-angle spinning, and total suppression of spinning sidebands (CP/MAS/TOSS) was utilized. The NMR measurement conditions were: contact time, 2 ms; data points, 2048; relaxation delay, 1–2 s; spinning rate, 5 kHz; and decoupling method, two-pulse phase-modulation. All NMR spectra were externally referenced by setting the methyl peak of hexamethyl benzene to 17.3 ppm.

Characterization of the PBC nanoparticles in the SD suspensions

DLS measurement. The MV of the particles in the suspensions was determined with a Microtrac UPA® (MicrotracBEL Corp., Japan; measurement range, 0.0008–6.5 μm), with a wavelength of 780 nm, laser power of 3 mW, and a heterodyne detector. The detector signal was digitized, and the frequency power spectrum of the signal was recorded using fast Fourier transform digital

signal processing. Measurements were acquired under the following conditions: reflected light intensity, 281.4 mV; measurement time, 60 s; and repeat count, 3 times. Approximately 450 μL of the sample suspension was added to the DLS cell. The polydispersity index (PDI) was calculated using equations (1) and (2) as per MicrotracBEL Corp., Japan (ISO 22412:2008). X_{DLS} (μm) and $\Delta Q_{int,\,i}$ indicate the average hydrodynamic diameter and intensity-weighted amount of particles with size X_{i} arbitrary units, respectively.

$$\overline{x_{\mathrm{DLS}}} = \frac{\sum_{i=1}^{N} \Delta Q_{\mathrm{int},i}}{\sum_{i=1}^{N} \frac{\Delta Q_{\mathrm{int},i}}{x_i}} \quad \cdots\cdots \quad (1)$$

$$\mathrm{PDI} = 2\overline{x_{\mathrm{DLS}}}^{2} \frac{\sum_{i=1}^{N} \Delta Q_{\mathrm{int},i} \left(1/x_i^2 - 1/\overline{x_{\mathrm{DLS}}}^{2} \right)}{\sum_{i=1}^{N} \Delta Q_{\mathrm{int},i}} \quad \cdots\cdots \quad (2)$$

Cryo-TEM measurement. Cryo-TEM measurements were acquired with an accelerating voltage of 120 kV on a JEM-2100F field emission TEM apparatus (JEOL Co., Ltd., Japan). For cryo-TEM, 2 μL of the prepared suspension was deposited on a 200-mesh copper grid covered with holey carbon film (Nisshin EM Co., Ltd, Tokyo, Japan). A thin aqueous film (*ca.* 100 nm thick) of the nanoparticle suspension was prepared by blotting the excess liquid. Further, the film was rapidly vitrified by immersion in liquid ethane using a Leica CPSC cryo-preparation chamber (Leica Microsystems. Wetzlar, Germany). The grid with the vitrified thin film was set on a sample holder and transferred to the microscope chamber. The sample temperature was kept below −170 °C using liquid nitrogen. Images were captured with a CCD camera. ImageJ software (National Institutes of Health, USA) was used to carry out statistical analysis of the particle diameter and roundness observed in the cryo-TEM images. At least 30 images of each sample were captured at

different locations; the most representative images were shown to present the general trend observed. More than 300 particles in the images were recorded and utilized for statistical analysis. The particle diameter is defined as the longest distance between any two points along the selection boundary of the particle. Roundness with a value of 1.0 indicates a perfect circle. As the value approaches 0.0, this indicates an increasingly elongated shape. The roundness value of selected particles was calculated using equation (3).

$$\text{Roundness} = 4 \times \frac{[Area]}{\pi \times [Major\ axis]\ 2} \qquad \cdots\cdots \quad (3)$$

RESULT AND DISCUSSION

PART I. IMPACT OF PREPARATION METHODS OF TERNARY SOLID DISPERSIONS ON THE PHYSICAL STABILITY OF PBC AMORPHOUS DRUG NANOPARTICLES

Characterization of the spray-dried sample (SPD) and the ground mixtures (GMs)

Powder X-ray diffraction (PXRD) measurements.

PXRD measurements were performed to evaluate the crystallinity of probucol (PBC) in the SPD and GMs. The spray-dried PBC (Figure 2b) exhibited a PXRD pattern consistent with that reported for metastable PBC (form II). The SDS (Figure 2d) showed an overlapping diffraction pattern corresponding to its hydrate and anhydrate forms.[30] The spray-dried SDS showed a diffraction pattern corresponding to its hydrate form (Figure 2e). In the diffraction pattern of the SPD (Figure 2f), only the characteristic peaks of the SDS hydrate form were detected; peaks corresponding to crystalline PBC were not observed. No crystalline PBC peaks were observed in either of the diffraction patterns of the GMs (Figure 2g,h), and only the diffraction peaks of the anhydrate form of SDS remained. Therefore, judging from the PXRD measurements, PBC was amorphized by spray drying and co-grinding with hypromellose (HPMC) and sodium dodecyl sulfate (SDS).

Solid-state ^{13}C nuclear magnetic resonance (NMR) spectroscopy.

In order to characterize the crystallinity of PBC in the SPDs and GMs, solid-state ^{13}C NMR spectroscopy was also utilized.[22] Figures 3 and 4 show an expansion of the solid-state ^{13}C NMR

spectra (from 115 to 160 ppm) and the full spectra (from 0 to 200 ppm), respectively. The characteristic peaks of PBC were completely broadened in the solid-state ^{13}C NMR spectra of both the SPD and GM samples (Figure 3c−e). The peak broadening indicated a wide distribution of isotropic chemical shifts resulting from the higher disorder of the amorphous materials.[31] Therefore, judging by solid-state NMR spectroscopy, which detects atomic level information, PBC was also amorphized by spray drying and co-grinding with HPMC and SDS, corresponding to the PXRD results.

DSC measurements.

DSC measurements were carried out to evaluate the crystallization behavior of PBC during the heating process (Figure 5). The melting peaks for PBC (form I) and (form II), which have an enantiotropic relationship, were observed at 124.3 and 114.2 °C, respectively (Figure 5a,b), in agreement with previously reported data.[32] In both the unprocessed and spray-dried SDS samples, the endothermic peak derived from the hydrate form was observed at approximately 90 °C (Figure 5d,e). The SPD (Figure 5f) showed a peak corresponding to the hydrate form of SDS at 94.7 °C. However, neither crystallization nor melting thermal events were detected for PBC. Thus, the amorphous state of PBC remained stable in the SPD during the heating process of the DSC experiments. On the other hand, the endothermic peaks observed in GM (I) and (II) were probably due to the melting of PBC at 120.9 and 112.5 °C, corresponding to PBC (form I) and (form II), respectively. The enthalpy values of the melting peaks of the crystalline PBC (ΔH) in GM (I) and (II) were 11.2 and 7.7 J/g, respectively, as calculated from the amount of PBC. These values were much lower than the 71.2 J/g observed for PBC (form I) and 67.7 J/g observed for PBC (form II). No glass transition can be observed even in the mDSC experiments on the SPD and GM samples

(data not shown). The absence of a glass transition could have been caused by the complicated combination of thermal events, including the glass transition, crystallization of PBC and SDS, and water desorption in this area. The broad endotherm ranging from 25−75 °C in the SPD, GM (I), and GM (II), DSC traces was primarily attributable to the endothermic peak of water desorption.

Variable-temperature PXRD measurements

PXRD measurements were carried out at various temperatures to verify the DSC results (Figure 6). In the SPD, no peaks corresponding to crystalline PBC were found at any temperature, and the amorphous PBC remained stable. On the other hand, diffraction peaks derived from PBC (form I) and (form II) were observed in GM (I) at 110 °C and GM (II) at 100 °C, respectively, indicating that some of the amorphous PBC in each GM had recrystallized to their initial crystal form during the heating process. In the spray-drying method, which is categorized as a bottom-up approach, a drug is first wholly dissolved in an organic solvent and then amorphized through solvent evaporation. Therefore, spray drying produced completely amorphized PBC that was homogeneously mixed into the HPMC matrix.[33] Thus, the amorphous PBC in SPD remained stable even upon heating. On the other hand, co-grinding, which is categorized as a top-down approach, gradually reduces the size of the drug crystals by a mechanical force, leading to amorphization. Herein, two possible hypotheses regarding the molecular state of the PBC in the GMs are suggested. In hypothesis (i), although almost all of the PBC was in an amorphous state after grinding, a minuscule amount of tiny PBC nuclei remained in the GMs.[34] In hypothesis (ii), the PBC was completely amorphized by grinding, but some of the PBC formed PBC-rich domains retained the short-range order of the initial crystal form.[35,36] These tiny PBC nuclei or PBC-rich domains induced crystallization (via nucleation and crystal growth) upon heating, resulting in the

appearance of crystalline PBC peaks in the DSC curves and variable temperature PXRD patterns. Notably, according to the ΔH value in the DSC curve, the amount of crystallized PBC produced during heating was small, and almost all of the PBC remained in the amorphous state even after heating. It is hard to determine the molecular state of PBC in the GMs at this stage, i.e., whether a minuscule amount of tiny PBC nuclei or PBC-rich domains were present; however, the different thermodynamic stabilities of the SPDs and the GMs were confirmed.

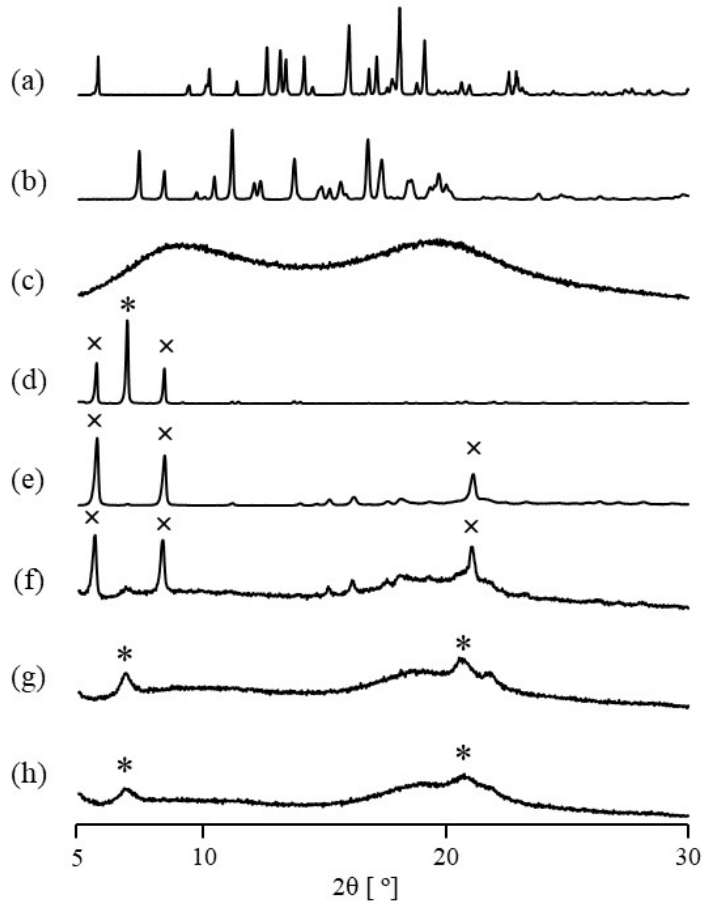

Figure 2. PXRD patterns of (a) PBC (form I), (b) PBC (form II), (c) HPMC, (d) SDS, (e) spray-dried SDS, (f) SPD, (g) GM (I), and (h) GM (II). Characteristic peaks of the (×) PBC (form I), (□) PBC (form II), (□) SDS anhydrate, and (×) SDS hydrate.

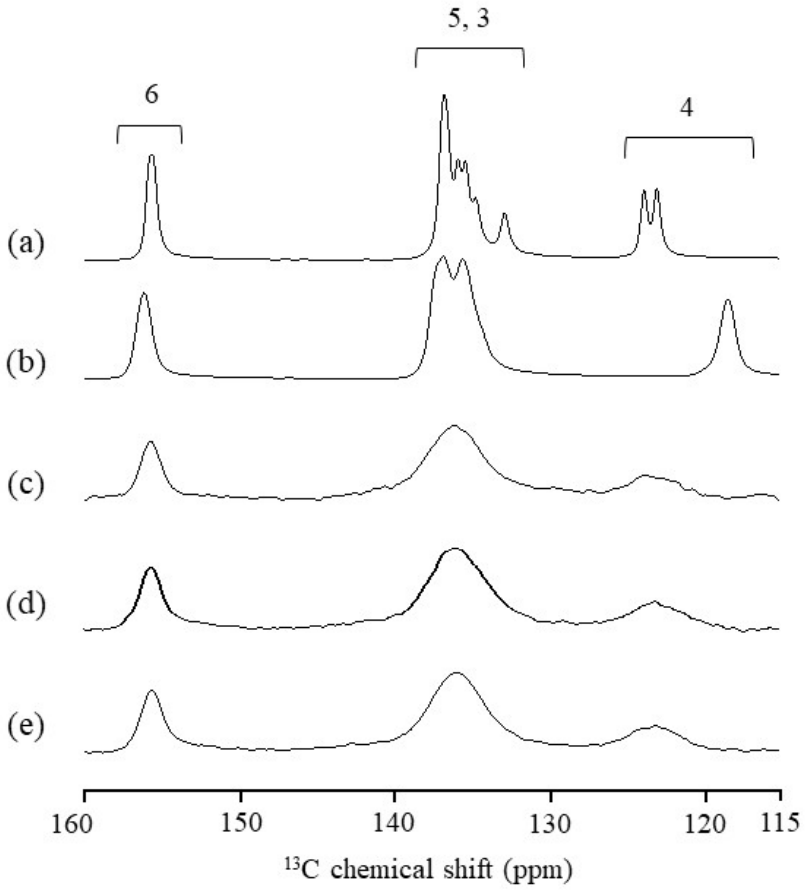

Figure 3. Solid-state ^{13}C NMR spectra (115−160 ppm) of (a) PBC (form I), (b) PBC (form II), (c) SPD, (d) GM (I), and (e) GM (II).

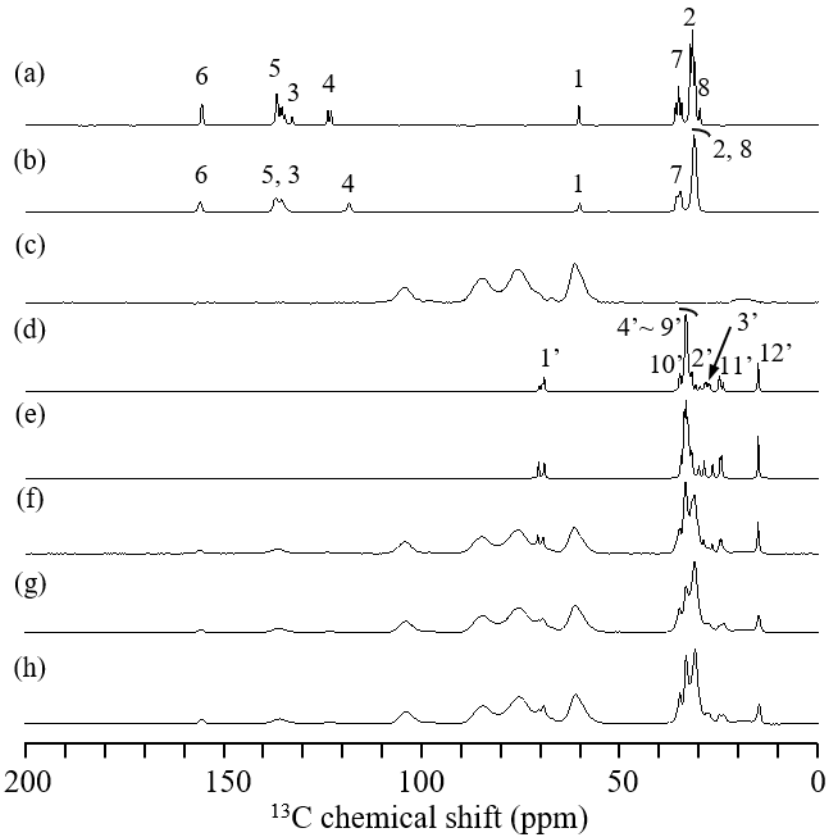

Figure 4. Full solid-state ^{13}C NMR spectra (0–200 ppm) of (a) PBC (form I), (b) PBC (form II), (c) HPMC, (d) SDS, (e) spray-dried SDS, (f) SPD, (g) GM (I), and (h) GM (II).

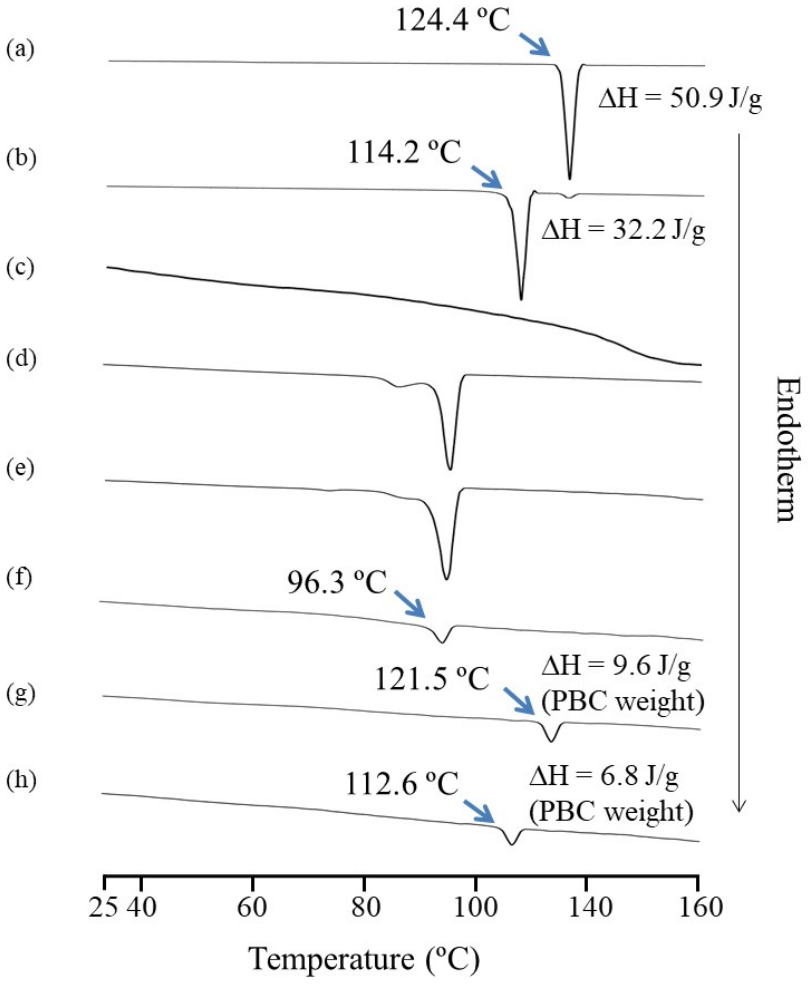

Figure 5. DSC curves of (a) PBC (form I), (b) PBC (form II), (c) HPMC, (d) SDS, (e) spray-dried SDS, (f) SPD, (g) GM (I), and (h) GM (II). The enthalpies of the melting peaks of crystalline PBC (ΔH) are given in the figure.

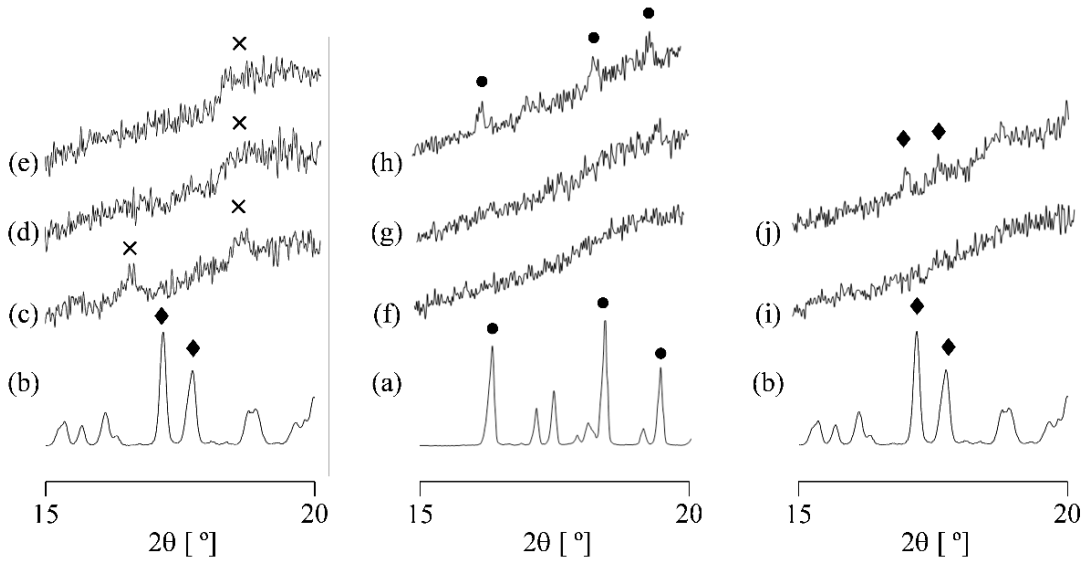

Figure 6. PXRD patterns of (a) PBC (form I), (b) PBC (form II), (c−e) SPD (at 25, 100, and 110 °C), (f−h) GM (I) (at 25, 100, and 110 °C), and (i, j) GM (II) (at 25 and 100 °C). Characteristic peaks of (●) PBC (form I), (♦) PBC (form II), and (×) SDS hydrate are denoted in the PXRD patterns.

Characterization of the SPD and GM suspensions

Particle size distribution.

DLS analysis (Figure 7) was used to monitor the changes in particle diameters for the particle size distributions of all the SPD and GM suspensions before and after storage at 40 °C. The successful formation of tiny nanoparticles with mean volume diameters (MVs) below 30 nm was confirmed in the freshly prepared SPD and GM suspensions. The suspensions showed unimodal size distribution patterns with a PDI of 0.09−0.12 (Figures 7a,f,k). In pharmaceutical nanoparticles, a PDI below ca. 0.10 is desired and indicates the monodispersity of the drug nanoparticles.[37] In the SPD suspension, although the size of the PBC nanoparticles gradually increased to ca. 140 nm after storage for 12 days, the particle size distribution of the nanoparticles remained unimodal (Figure 7a−e). The PDI decreased from 0.12 to 0.05 within 12 days of storage, showing that the particle size distribution became narrower over time. A gradual increase in the size of the nanoparticles and a decrease in the PDI were also observed for both GM suspensions after 1 day of storage (Figure 7g, l). However, both the GM suspensions formed some fraction of micrometer-sized precipitates after storage for 4 days and 8 days, as highlighted by the arrows (Figure 7h−i, m−n). Corresponding to the DLS analysis results, a small number of precipitates was observed with the naked eye. After 12 days of storage, the nanoparticles disappeared in the particle size distribution pattern, and only micrometer-sized particles were observed. Thus, the stabilities of the SPD and GM suspensions were quite different.

Quantification of the nanoparticles (<0.45 μm).

Next, the amount of PBC in the nanoparticles (<0.45 μm) at each storage time point was evaluated using HPLC (Figure 8). Considering that the reported solubilities of crystal and

amorphous PBC in water are 5 ng/mL and less than 1 μg/ mL[26], respectively, the dissolved component of PBC was negligible against the loaded concentration at 500 μg/mL. Hence, the PBC concentration in the filtrate almost wholly consisted of nanoparticles. Quantitative determination of the SPD suspension just after dispersion revealed that close to 100% of the loaded PBC existed as nanoparticles smaller than 0.45 μm. Furthermore, the PBC concentration remained constant throughout all 12 days of storage. Almost 100% of the PBC in both of the GM suspensions was incorporated into the nanoparticles initially and after 1 day of storage. However, the percentage of PBC in the filtrate of the GM suspensions decreased to 70% after storage for 4 days and to less than 10% after storage for 12 days. Thus, the SPD suspensions were quantitatively confirmed to have superior stability compared with the GM suspensions.

Cryogenic transmission electron microscopy (cryo-TEM) measurements.

Cryo-TEM was utilized to observe the changes in the size and shape of the nanoparticles because it can nearly reflect the nanometer-scale morphology of each nanoparticle in the suspended state.[38] Figure 9a−e shows the cryo-TEM images of the SPD suspensions after storage at 40 °C for 0−12 days. All the nanoparticles observed in the SPD suspension after storage for 0, 1, 4, and 8 days were spherical. After storage for 12 days, small amounts of needle-like nanoparticles were found, although most of the nanoparticles were still spherical. The mean number diameter (MN) of 100 spherical nanoparticles in the cryo-TEM images (Table 1) gradually increased during storage, supporting the DLS results. However, the size was slightly smaller than that determined from the DLS measurements (Figure 7). The possible reason is that TEM provides the actual particle size, whereas DLS reflects the hydrodynamic diameter.[39] In the TEM measurements, only the electron-rich inner core of the particle can be observed in the image. In comparison, the

polymer or surfactant covering on the nanoparticles affects the light scattering in the DLS analysis. Hence, the DLS results are a reflection of both the inner core and the shell layer. The MN from TEM analysis was converted to the MV to define the radius of gyration (Rg), and the Rg/hydrodynamic radius (Rh) value, which provides information on particle structure (Table 2), was calculated. The Rg/Rh value of the nanoparticles in the SPD suspension at each time point of storage ranged from 0.73 to 0.84. These values are close to 0.77, confirming that the nanoparticles were dense spheres.

The GM (I) suspension was composed of only spherical nanoparticles after short-term storage for 0−1 days (Figure 9f,g). However, after 4 days, in addition to the spherical nanoparticles, needle-like nanoparticles were also observed (Figure 9h). These needle-like nanoparticles showed higher contrast compared with the spherical nanoparticles. Furthermore, bright diffraction was observed on the sides of the particles, demonstrating their crystalline character.[38] BrozekMucha and Was-Gubala reported that cubic ice crystals, which have quite a similar morphology to that of the needle-like nanocrystals, can appear under exposure to the electron beam in cryo-TEM operation.[40] To confirm that these needle-like nanocrystals in Figure 9 are attributed to the sample and not the reported cryo-TEM artifact ice, the freeze-dried precipitates in the GM suspensions were characterized using TEM imaging (Figure 10). Some needle-like nanocrystals, which shared a similar morphology to those observed in the cryo-TEM images, appeared in the TEM images. It was confirmed that the needle-like nanocrystals were attributable to the sample generated in the GM suspensions upon storage. The coexistence of spherical nanoparticles and needle-like nanocrystals was also observed after 8 days of storage (Figure 9i). Also, using low magnification to obtain a broader visual field, micrometer-sized hexagonal crystals were detected, as highlighted

by the arrow (Figure 9j). The size of the spherical nanoparticles in the GM (I) suspension increased during storage, and their size was similar to that observed in the SPD suspension (Table 1). After 12 days of storage, neither the spherical nanoparticles nor needle-like nanocrystals were observed, and only micrometer-sized crystals were found (Figure 9k). The Rg/Rh values (approximately 0.77−0.78) of nanoparticles in the GM (I) suspensions stored for 0 and 1 day (Table 2) were close to 0.77, confirming their dense spherical structure. The Rg and Rh values of the GM suspensions after storage for 4 days or longer are not shown because the evaluation was difficult due to the various sizes and morphologies of particles.

In the GM (II) suspension, the similar nanoparticle evolution to that of the GM (I) suspension was observed during storage (Figure 9l−q); three distinct morphologies with different sizes were apparent, spherical nanoparticles that gradually increased in size (Table 1), needle-like nanocrystals, and micrometer-sized crystals. However, notably, the shape of the micrometer-sized crystals in the GM (II) suspension after storage for 8 days and 12 days was rod-like (Figure 9p, q), unlike the micrometer-sized hexagonal crystals observed in the GM (I) suspension. The significant differences in the shapes of micrometer-sized crystals in the GM (I) and GM (II) suspensions suggested generation of PBC different crystal forms in the two GM suspensions. The cryo-TEM images exhibited various particles of different sizes and shapes, including spherical nanoparticles, needle-like nanocrystals, and hexagonal and rod-like micrometer-sized crystals. Thus, the results provided a comprehensive understanding of the nanoparticles' evolution in the suspensions during storage.

PXRD Measurements of FDs.

For evaluating the crystallinity of PBC in each suspension at each storage time point, the

suspensions were freeze-dried and characterized by PXRD measurements (Figure 11). No characteristic peaks of crystalline PBC were observed in the FD prepared from the SPD suspension just after aqueous dispersion (Figure 11a), indicating the amorphous state of PBC at the initial time point. The halo pattern of PBC was maintained almost entirely during the 12 days of storage, but a small amount of PBC crystallization did occur (Figure 11a−e). It was speculated that although the morphology of the PBC nanoparticle remained spherical, crystallization of PBC gradually occurred inside the nanoparticle, as reported by Egami et al. [25]

For the FDs of the GM suspensions, small characteristic peaks of crystalline PBC were observed just after dispersion (Figure 11f, k). Almost all of the PBC in the nanoparticles was in the amorphous state, but a small amount of the crystalline phase was present. The intensity of the characteristic PBC peaks did not increase after 1 day of storage (Figure 11g, l). However, after storage for 4 days, the crystalline peaks of PBC (form I) and PBC (form II) were detected in the FDs of the GM (I) and GM (II) suspensions (Figure 11h, m), respectively, indicating that some of the PBC in the nanoparticles had reverted to its initial crystal form. Besides, the intensity of the crystalline peaks of PBC dramatically increased in the FDs between day 4 and day 12 of storage (Figure 11h−j, m−o), which likely reflected the growth of the PBC crystals. Both GMs could form nanoparticles just after dispersion when almost all the PBC was in the amorphous state. However, small amounts of PBC crystal phase in the nanoparticles induced their crystallization to their initial crystal forms.

Topographical imaging and force-distance curves analysis of atomic force microscopy (AFM) measurements.

The spherical nanoparticles in each suspension were evaluated immediately after dispersion

using AFM in tapping mode. Figure 12a−c shows the AFM height images of the nanoparticles in each suspension. In all suspensions, the particles were circular, which was consistent with the cryo-TEM images. In Figure 12d−f, the cross-sectional profiles show nanoparticles of 20−30 nm height and 50−70 nm width, except for a small amount of relatively larger nanoparticles. The width of the nanoparticles was overestimated because of AFM probe convolution effects (Figure 13). In this study, the widths of the nanoparticles in the AFM images were calculated using the simple model shown in Figure 13. The width calculated using the tip shape and average height of the nanoparticles was 48−63 nm, close to the measured width of 50−70 nm. Therefore, the nanoparticles should have retained their spherical morphology during AFM imaging. After taking the height images using the tapping mode, AFM force−distance curve measurements were carried out for 50 particles in each suspension immediately after aqueous dispersion using the contact mode to examine their mechanical properties. The probe approached the nanoparticles until the maximum force load reached 5 nN. Representative approach/retract cycles in the force−distance curves of each suspension are presented in Figure 12g−i. The distance between the contact points and substrate for all the force−distance curves for the SPD and GM suspensions was consistent with the height of the nanoparticles shown in the cross-sectional profiles (Figures 12d−f). This result confirmed that the force−distance curves were recorded for the centers of the nanoparticles (at least for the centers of the nanoparticles at the initial time point).

For the force−distance curves of the selected SPD nanoparticles (Figure 12g), all the approach curves had extremely low slopes despite the difference in particle sizes. This finding suggested that the nanoparticles in the SPD suspension formed a much softer structure. The force almost linearly increased for movement from the contact points to the substrate suggesting the elastic

deformation of nanoparticles during compression. The retraction of the tip induced the stretching of the nanoparticles. The maximum adhesive force was less than 0.2 nN, which also suggested the incredibly soft structure of the nanoparticles. The tip should have plunged into the nanoparticle instead of slipping to the side of the sample because a long-range continuous dissipation was observed in the retract curve.

On the other hand, the nanoparticles in the GM suspensions (Figure 12h, i) exhibited AFM force−distance curves rather different from those for the SPD suspension. The approach curves of the GM suspensions were atypical, showing an initial gradual slope after the contact point and a sudden force increase until the tip reached the substrate. The gradual slope was attributed to the slight deformation caused by compression or a soft "shell" of HPMC and SDS on the central PBC rich "core". Then, the tip approached and pressed the "core", which had a much higher stiffness. When the tip squished and plunged into the nanoparticles, more forces could act on the tip. This effect suggested a lower elasticity and a higher rigidity of the nanoparticles in the GM suspensions than those of the SPD suspension particles. Finally, the tip reached the substrate surface, and the force showed a vertical rise. The first part of the retract curves, when the tip gradually separated from the substrate, overlapped with the approach curves without hysteresis. A more potent maximum adhesive force above 0.5 nN also indicated a stiffer structure of the nanoparticles in the GM suspensions.

These results of the AFM force−distance curves clearly showed that the nanoparticles in the GM suspensions were stiffer than those in the SPD suspensions immediately after dispersion. The most likely reasons for this difference in stiffness of the nanoparticles observed in the SPD and two GM suspensions were the various molecular states of PBC and the various compositions

contained in the nanoparticles, which may have subsequently affected the stability of nanoparticles over time.

Quantitative evaluation of HPMC and SDS concentration in the liquid phase.

The quantitative evaluation of HPMC and SDS concentrations in the liquid phase of freshly prepared SPD and GM suspensions was conducted using solution-state ^{1}H NMR measurements (Table 3). The PBC peak was not observed because of the extremely low concentration of dissolved PBC in the suspension. For the freshly prepared SPD suspension, the concentration of HPMC decreased to 1.73 mg/mL (86.3%); whereas that of SDS was 0.96 mg/mL (96.0%). Similarly, the HPMC and SDS concentrations in the liquid phase of the GM (I) and GM (II) suspensions were also close to 85 and 95%, respectively. This result indicated that the weight ratio of PBC/HPMC/SDS in the nanoparticles was close to 1:0.55:0.1. Hence, most of the HPMC and SDS were freely dissolved in the solution. The crystallization of supersaturated PBC may have been inhibited by interactions with the dissolved HPMC via noncovalent interactions.[41] Other HPMCs, which can localize in the cores of nanoparticles and at the interface, play crucial roles in preventing the nanoparticles from undergoing crystallization and aggregation/ agglomeration, respectively. The SDS covering at the interface of the amorphous drug nanoparticles also inhibits the aggregation/agglomeration via charge repulsion, which was evidenced by the zeta potentials (Table 4). Previously, Egami et al. reported that the ratio of PBC/HPMC/SDS in nanoparticles prepared using a PBC/HPMC/SDS = 1:1.75:1.25 SPD that was 1:0.4:0.04, suggesting a lower ratio of HPMC and SDS in the nanoparticles than that obtained using the PBC/HPMC/SDS = 1:4:2 SPD in this study. This finding can explain why the nanoparticles in the present SPD suspension are more stable than those in the former SPD suspension. The consistency between the

dissolved concentrations of HPMC and SDS in the SPD and two GM suspensions suggests that different mechanical properties did not result from the different concentrations of HPMC contained in the nanoparticles but from the different molecular states of PBC in the nanoparticles. Therefore, it is more likely that the PBC crystal phase was present inside the nanoparticles in the GM suspensions. The PBC in the nanoparticles of the SPD suspension was completely in the amorphous state. These results were in agreement with the PXRD results of the FDs of the suspensions immediately after dispersion.

Considering the extremely small forces in the AFM force-distance curves, the nanoparticles in both the SPD and GM suspension formed a soft structure. All or almost all of the PBC in the nanoparticles of the SPD or GM suspensions existed in an amorphous state. The amorphous state of PBC in the nanoparticles may be a supercooled-liquid state rather than a glass state (discussed in the later section). Therefore, the nanoparticles in the SPD suspension, wherein the PBC was entirely in a supercooled-liquid state, were loose and soft. Hence, extremely small forces worked on the tip both in the approach and the retraction processes. On the other hand, a small amount of PBC crystal phase was generated in the nanoparticles of the GM suspensions. This phase could have made the nanoparticles slightly harder, and hence, the tip required more force for the approach and retraction processes.

The significant differences in the shapes of the hexagonal and rod-like micrometer-sized crystals observed after long-term storage in the GM (I) and GM (II) suspensions were believed to correspond to the different crystal forms of PBC. Therefore, the GM (I) and GM (II) suspensions were centrifuged at 1000g for 20 min after storage for 8 days at 40 °C, followed by a freeze-drying process. The obtained precipitates of the GM (I) and GM (II) suspensions were

evaluated by microscopy and PXRD analysis.

TEM measurements of micrometer-sized precipitates

TEM imaging (Figure 14a,b) was conducted on the micrometer-sized precipitates to determine their morphologies. Micrometer-sized hexagonal and approximately rod-like crystals were observed in the precipitates of the GM (I) and GM (II) suspensions, respectively, which corresponded with the morphology of micrometer-sized crystals in the cryo-TEM images (Figure 9). Thus, the micrometer-sized precipitates obtained from the GM (I) and GM (II) suspensions could be attributed to PBC (form I) and PBC (form II) crystals, respectively. The PXRD patterns in Figure 11c,d indicated that the crystalline peaks of the micrometer-sized precipitates from the GM (I) and GM (II) suspensions were consistent with the characteristic peaks of PBC (form I) and PBC (form II) crystals, respectively. This finding further confirmed that the PBC in the nanoparticles prepared from the GMs induced their crystallization to their initial PBC crystal form.

Notably, both cryo-TEM and TEM imaging revealed that these micrometer-sized precipitates were not secondary particles but were primary particles. Hence, no intermediates corresponding to aggregation or agglomeration were formed during the entire storage period. This finding demonstrated that the micrometer-sized crystals were formed from the needle-like nanocrystals by solution-phase-mediated crystal growth.

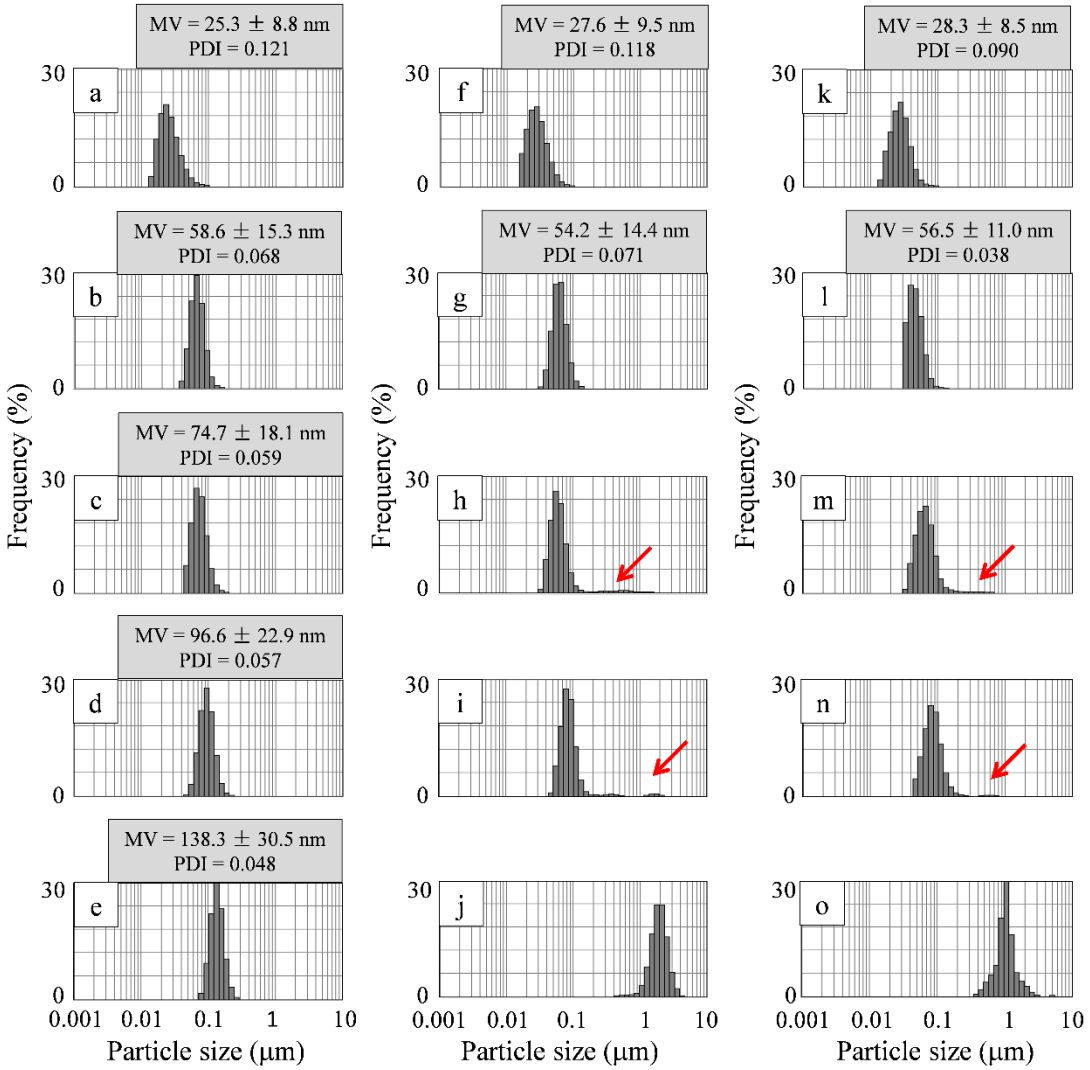

Figure 7. Particle size distribution patterns determined by DLS of the (a–e) SPD suspension, (f–j) GM (I) suspension, and (k–o) GM (II) suspension after storage at 40 °C for (a, f, k) 0 days, (b, g, l) 1 day, (c, h, m) 4 days, (d, i, n) 8 days, and (e, j, o) 12 days. The MV (n = 3, mean ± S.D.) and PDI are also shown in the figure. The arrows indicate the micrometer-sized precipitates in the suspensions.

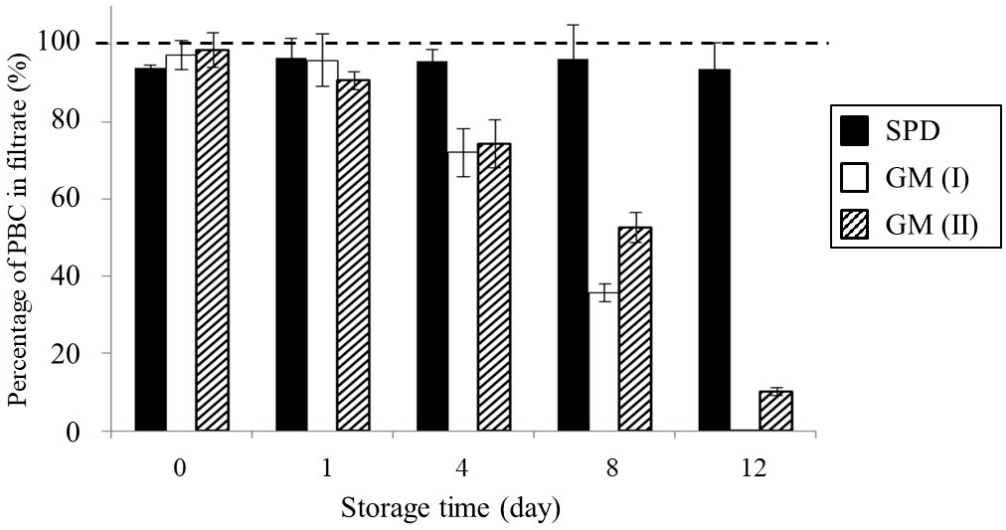

Figure 8. Percentage of PBC in the filtrate of each suspension after storage at 40 °C (n = 3, mean ± S.D.).

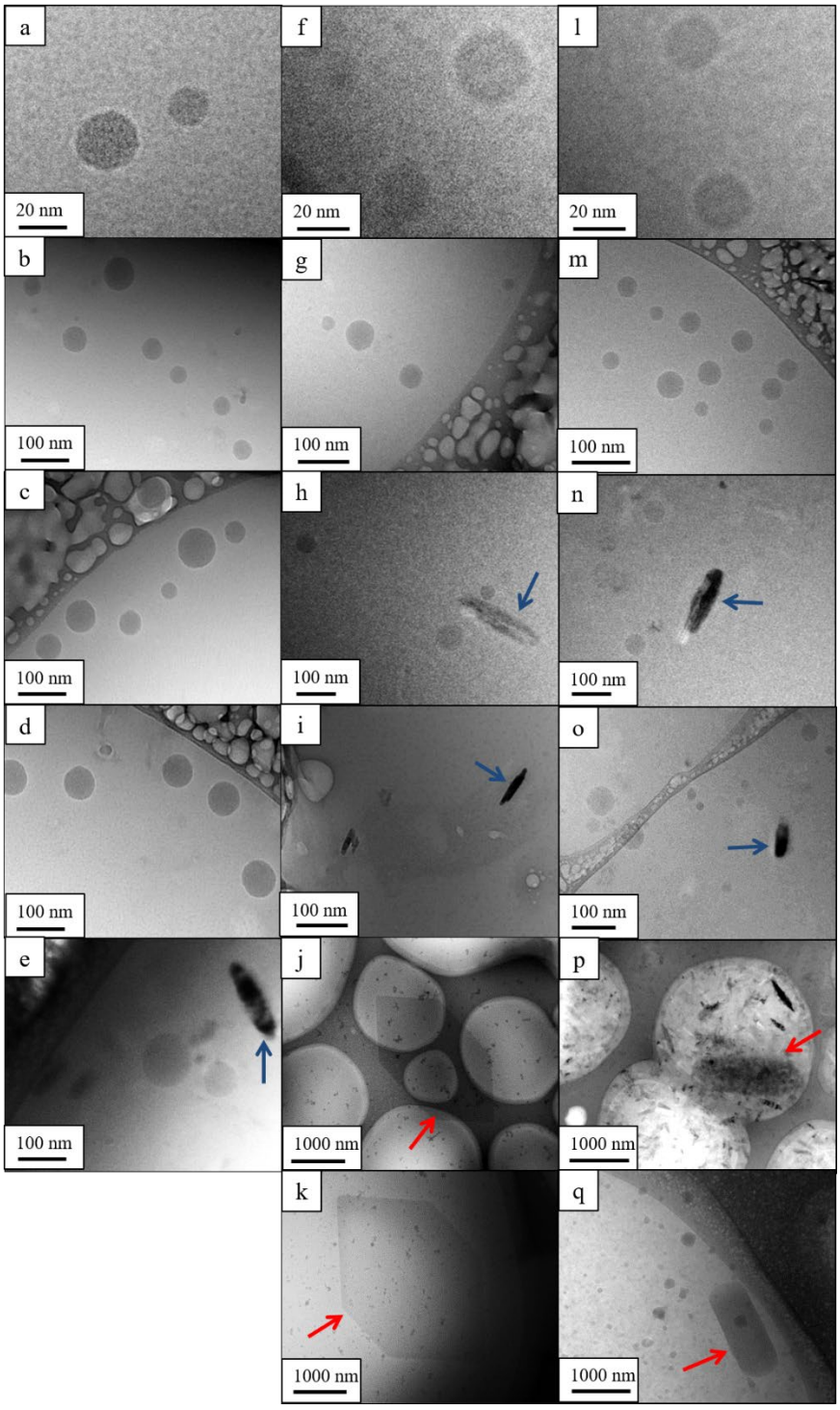

Figure 9. Cryo-TEM images of the (a−e) SPD suspension, (f−k) GM (I) suspension, and (l−q) GM (II) suspension after storage at 40° C for (a, f, l) 0 days, (b, g, m) 1 day, (c, h, n) 4 days, (d, i−j, o−p) 8 days, and (e, k, q) 12 days. The cyan arrows in (e), (h), (i), (n), and (o) highlight needle-like nanocrystals. The red arrows in (j−k) and (p−q) point to micrometer-sized hexagonal crystals and micrometer-sized rod-like crystals, respectively.

Table 1. The mean number diameter (MN) of the spherical nanoparticles in each suspension observed in cryo-TEM images. (Mean ± S.D, n = 100)

MN diameter (nm)	Storage time (day)				
	0	1	4	8	12
SPD suspension	14.1 ± 4.3	36.1 ± 10.1	55.7 ± 14.9	70.7 ± 17.0	110.6 ± 18.8
GM (I) suspension	17.0 ± 6.5	37.1 ± 10.7	58.8 ± 15.6	65.6 ± 16.3	—
GM (II) suspension	13.0 ± 8.4	41.6 ± 13.2	53.1 ± 20.6	77.6 ± 12.3	121.8 ± 23.0

Table 2. Radii of gyration, R_g, hydrodynamic radii, R_h, and the ratio of R_g/R_h for SPD, GM (I), and GM (II) suspensions after storage for 0, 1, 4, 8, and 12 days. The R_g was determined by converting the MN from cryo-TEM images to the MV, and the R_h was determined by DLS analysis.

Sample	Storage time (day)														
	0			1			4			8			12		
	R_g (nm)	R_h (nm)	R_g/R_h	R_g (nm)	R_h (nm)	R_g/R_h	R_g (nm)	R_h (nm)	R_g/R_h	R_g (nm)	R_h (nm)	R_g/R_h	R_g (nm)	R_h (nm)	R_g/R_h
SPD suspension	9.3	12.7	0.73	22.4	29.3	0.76	31.2	37.4	0.83	39.3	48.3	0.81	58.3	69.2	0.84
GM (I) suspension	10.8	13.8	0.78	21.3	17.1	0.78	–	–	–	–	–	–	–	–	–
GM (II) suspension	10.9	14.2	0.77	22.2	28.3	0.78	–	–	–	–	–	–	–	–	–

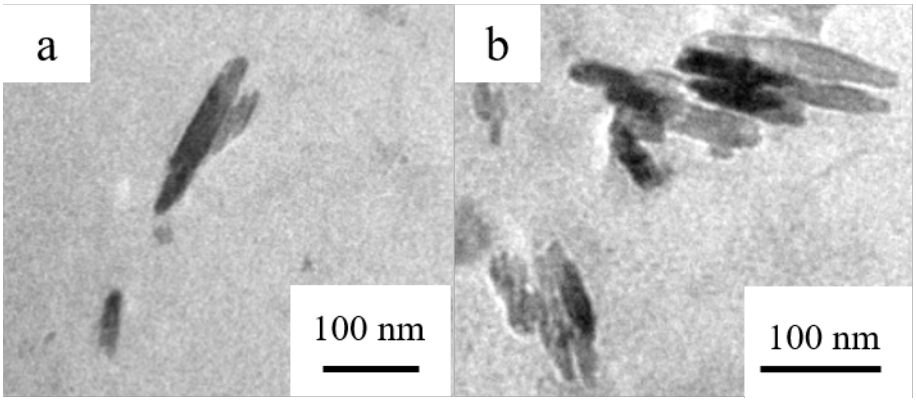

Figure 10. TEM images of needle-like nanocrystals in freeze-dried precipitates of (a) GM (I) and (b) GM (II) suspensions after storage for 4 days.

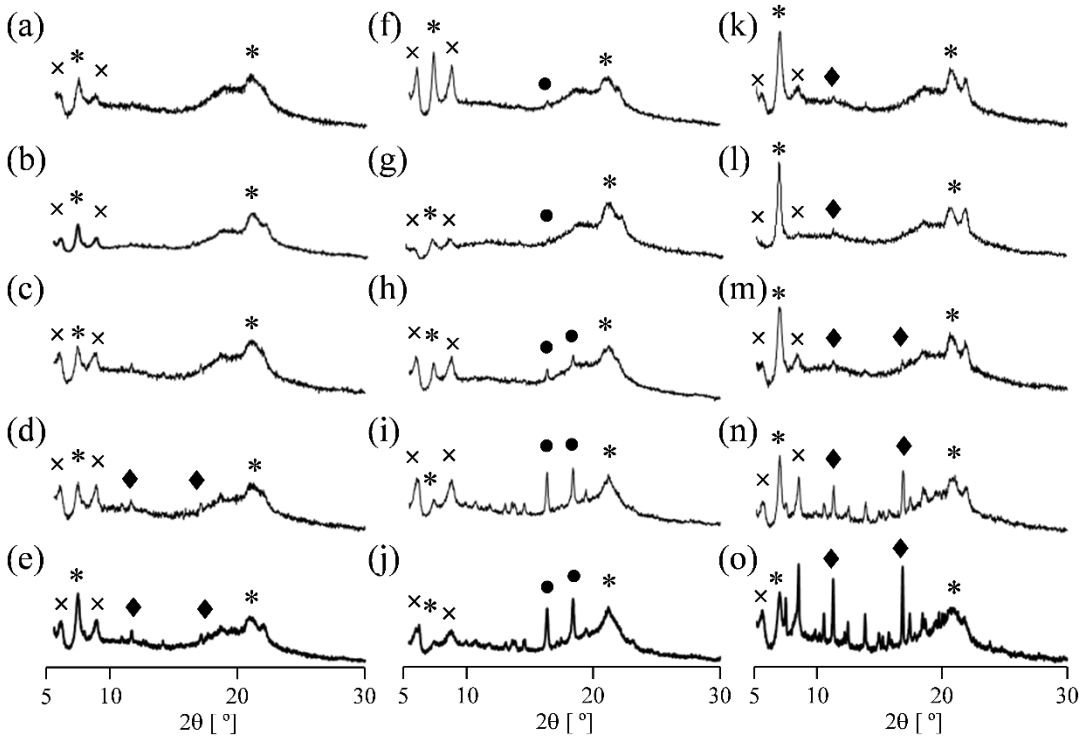

Figure 11. PXRD patterns of (a−e) the FDs of the SPD suspension, (f−j) the FDs of the GM (I) suspension, and (k−o) the FDs of the GM (II) suspension after storage for (a, f, k) 0 days, (b, g, l) 1 day, (c, h, m) 4 days, (d, i, n) 8 days, and (e, j, o) 12 days. Characteristic peaks of (•) PBC (form I), (⧫) PBC (form II), (*) SDS anhydrate, and (×) SDS hydrate are denoted in the PXRD patterns.

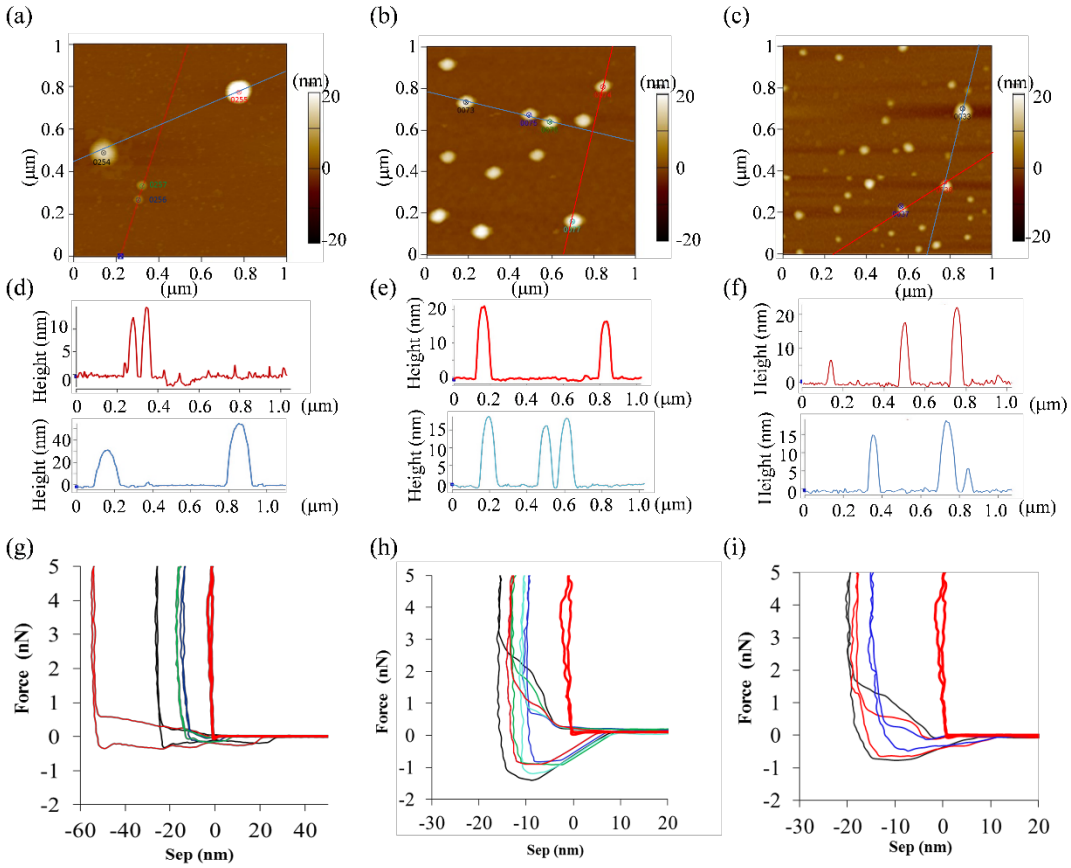

Figure 12. AFM height images of (a) SPD, (b) GM (I), and (c) GM (II) suspensions. The cross-sectional profiles analyzed for the red and cyan lines in (a–c) are shown in (d–f), respectively. (g–i) The force–distance curves were recorded for the selected points in the height images of (a–c), respectively. The colors of the force–distance curves correspond to the mark colors of the selected points were shown in (a–c).

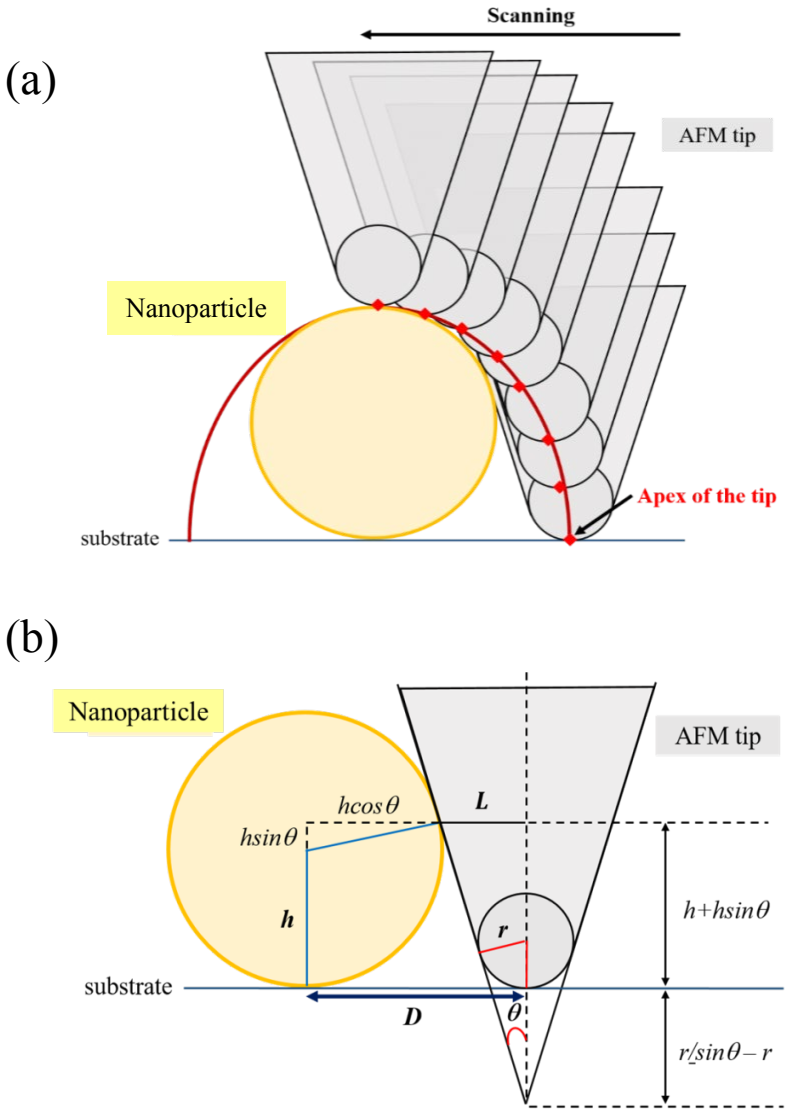

Figure 13. (a) A schematic illustration of AFM probe convolution effects. As the tip moves across the substrate, the sides of the tip come into contact with the sample before the apex does. Therefore, the width of the sample is broadened in the image, whereas the height is correct. (b) A schematic illustration of a calculation model of the apparent diameter of nanoparticles in AFM images.

Table 3. HPMC and SDS concentrations of freshly prepared SPD and GM suspensions determined via solution-state ^{1}H NMR measurements (n = 3; Mean ± S.D.)[a]

Calculated conc. (mg/mL)	SPD	GM (I)	GM (II)
HPMC	1.73 ± 0.06 (86.30 %)	1.73 ± 0.05 (86.33 %)	1.71 ± 0.02 (85.67 %)
SDS	0.96 ± 0.02 (96.00 %)	0.96 ± 0.03 (95.67 %)	0.93 ± 0.03 (93.00 %)

[a]Round brackets indicate the ratio of dissolved HPMC and SDS in the suspensions against the loaded concentration.

Table 4. Zeta potential of SPD, GM (I), and GM (II) suspensions immediately after aqueous dispersion determined using ELS Z1TY (Otsuka Electronics Co., Ltd, Japan) (n = 3, mean ± S.D.)

	Zeta potential (mV)
SPD suspension	-24.0±0.3
GM (I) suspension	-20.2±0.3
GM (II) suspension	-24.3±0.8

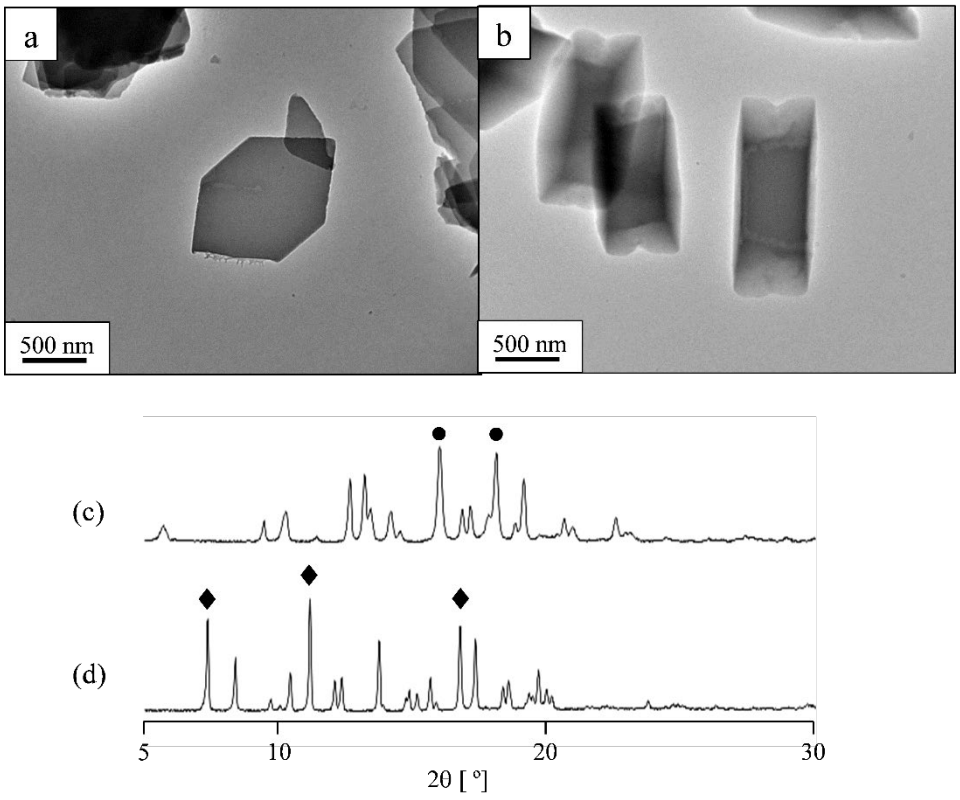

Figure 14. (a−b) TEM images and (c−d) PXRD patterns of the precipitates from the (a, c) GM (I) and (b, d) GM (II) suspensions after storage at 40 °C for 8 days. The characteristic peaks of (●) PBC (form I) and (♦) PBC (form II) are denoted in the PXRD patterns.

Discussion of nanoparticle evolution in aqueous solution.

Recently, Harmon et al. proposed a potential mechanism for nanoparticle formation in which, driven by exposure to water, an amorphous solid dispersion (SD) undergoes amorphous−amorphous phase separation and forms nanosized amorphous drug domains within the amorphous SD.[42] The entire process was observed via optical microscopy images. These amorphous drug domains are directly released into the bulk solution as drug nanoparticles. The polymer and surfactant play an essential role in the dissolution rate of the drug and the dispersibility of the nanoparticles, which highly affect the stability and size of the generated nanoparticles. This mechanism of nanoparticle generation can be used to explain the hypothesis that a small amount of PBC nuclei or PBC-rich domains with the short-range order of the initial crystal form remains in the spherical PBC nanoparticles just after their dispersion in water.

Combining the results and the hypothesis described above, the correlation between the molecular state of PBC in the SPD and GMs before and after being dispersed into water and the physical stability of the nanoparticles in water is discussed. The proposed evolution of the nanoparticles in water is summarized in Figure 15.

In the SPD prepared by the spray-drying method, the PBC was completely amorphized and homogeneously mixed with HPMC and SDS. PBC nucleation and crystal growth after being dispersed in water were effectively inhibited or delayed. The amorphous state of the PBC in the nanoparticles was maintained for a relatively long period. A similar observation regarding the evolution of amorphous nanoparticles has been reported by Ricarte et al. [26] The gradual increase in the particle size of spherical nanoparticles during storage in water could be due to Ostwald ripening. In Ostwald ripening, the differences in local solubility depending on the particle size

lead to the transport of drug molecules from small to larger particles. The size of the larger particles increases with time at the expense of the dissolution of smaller particles. In this study, the nanoparticles in the SPD suspension and those in both the GM suspensions exhibited an increase in particle size and a decrease in PDI after storage for 12 days and 1 day, respectively (Figure 7). The gradual increase in the particle size of the spherical nanoparticles was accompanied by a narrowing of the particle size distribution. The PDI values (approximately 0.09−0.12) of freshly prepared samples rapidly decreased to approximately 0.07 for the SPD suspension and GM (I) suspension and to 0.04 for the GM (II) suspension, for 1-day storage. The SPD samples showed a slower change in PDI values, from 0.07 for 1-day storage to 0.05 for 12-day storage. The driving force for Ostwald ripening was the difference in solubility between smaller and larger particles. A narrower particle size distribution resulted in a slower rate. Additionally, no secondary particles were observed in the cryo-TEM images. Therefore, Ostwald ripening, rather than aggregation/agglomeration, is the most reasonable explanation for the increasing particle size of the spherical nanoparticles in the SPD suspension. This explanation is in agreement with a previous study by Lindfors et al., who reported that amorphous drug nanosuspensions are prone to particle growth due to Ostwald ripening.[43] However, the amorphous PBC inside the spherical nanoparticles in water tended to crystallize to lower its high Gibbs free energy. The spherical shape of the nanoparticles was maintained even after the PBCs had crystallized, although further crystallization changed the morphology from spherical to a specific crystal shape. Egami et al. demonstrated the gradual crystallization process of PBC in nanoparticles by AFM force−distance curves.[25] Direct morphological observation of the nucleation pattern of amorphous nanoparticles is rare for organic compounds, although it has been reported for inorganic compounds.[44]

Furthermore, a recent study by Yamasaki et al. directly visualized the nucleation process of amorphous protein lysozyme nanoparticles by in situ cryo-TEM imaging.[45] The nucleation process of the lysozyme crystals was similar to that observed in the present study. However, the lysozyme molecules did not directly assemble into crystal nuclei; instead, their nucleation process followed the two-step or nonclassical nucleation theory. A liquid droplet composed of lysozymes was generated as an intermedium phase before the nucleation process and the crystalline nuclei then formed within these droplets.[46]

In contrast, the co-grinding method induced the amorphization of PBC by the gradual reduction of the drug crystal size by mechanical force. Hence, although almost all of the PBC was in an amorphous state, small amounts of PBC nuclei or PBC-rich domains with short-range order corresponding to the initial crystal form remained in GMs. Here, the molecular state of the PBC molecule just after the aqueous dispersion of the GMs is discussed. In this study, the storage temperature of the suspensions was 40 °C, which is higher than the reported glass transition temperature (T_g) of amorphous PBC (23 °C)[32]. HPMC, which has a T_g of approximately 160 °C, could enhance the T_g in the GMs, although most of the HPMC dissolved into the water after aqueous dispersion (Table 3). Furthermore, the T_g confinement effect due to the size reduction and the inclusion of water (Tg = −138 °C) in the nanoparticles could also reduce the Tg of the nanoparticles.[47−49] Therefore, the amorphous PBC in the nanoparticles in water was more likely in a supercooled liquid state than in a glass state. As demonstrated in the AFM force−distance curve measurement (Figure 12), the incredibly soft structure of the nanoparticles could be derived from this supercooled liquid state of PBC. Thus, it is unlikely that PBC-rich domains that retain the short-range order of the initial crystal forms were present within the nanoparticles in water

because such short-range order is quite challenging to maintain in the high-molecular-motility supercooled liquid state.[50] It could not be definitively determined whether tiny amounts of PBC nuclei or drug-rich domains with short-range order remained in the GMs. However, the crystallization (nucleation and crystal growth) of PBC occurred at the time of aqueous dispersion, resulting in the appearance of tiny X-ray peaks corresponding to crystalline PBC in the FDs of GM suspensions. Based on the AFM force−distance curves and cryo-TEM images, the crystal phase was present inside the spherical nanoparticles just after dispersion. The PBC nuclei grew inside the spherical nanoparticles during storage and then formed needle-like nanocrystals whose interface with water could be covered by HPMC and SDS. Once the crystal phase came into contact with the solution phase, the remaining amorphous nanoparticles became highly unstable, as reported by Lindfors et al.,[51] since the solubility of the amorphous phase is at least an order of magnitude higher than the corresponding crystalline solubility. As a consequence, the PBC in the amorphous nanoparticles spontaneously dissolved, while the nanocrystals grew in a similar manner to Ostwald ripening.[51] Finally, via solution-phase-mediated crystal growth, the needle-like nanocrystals became primary micrometer-sized crystals.

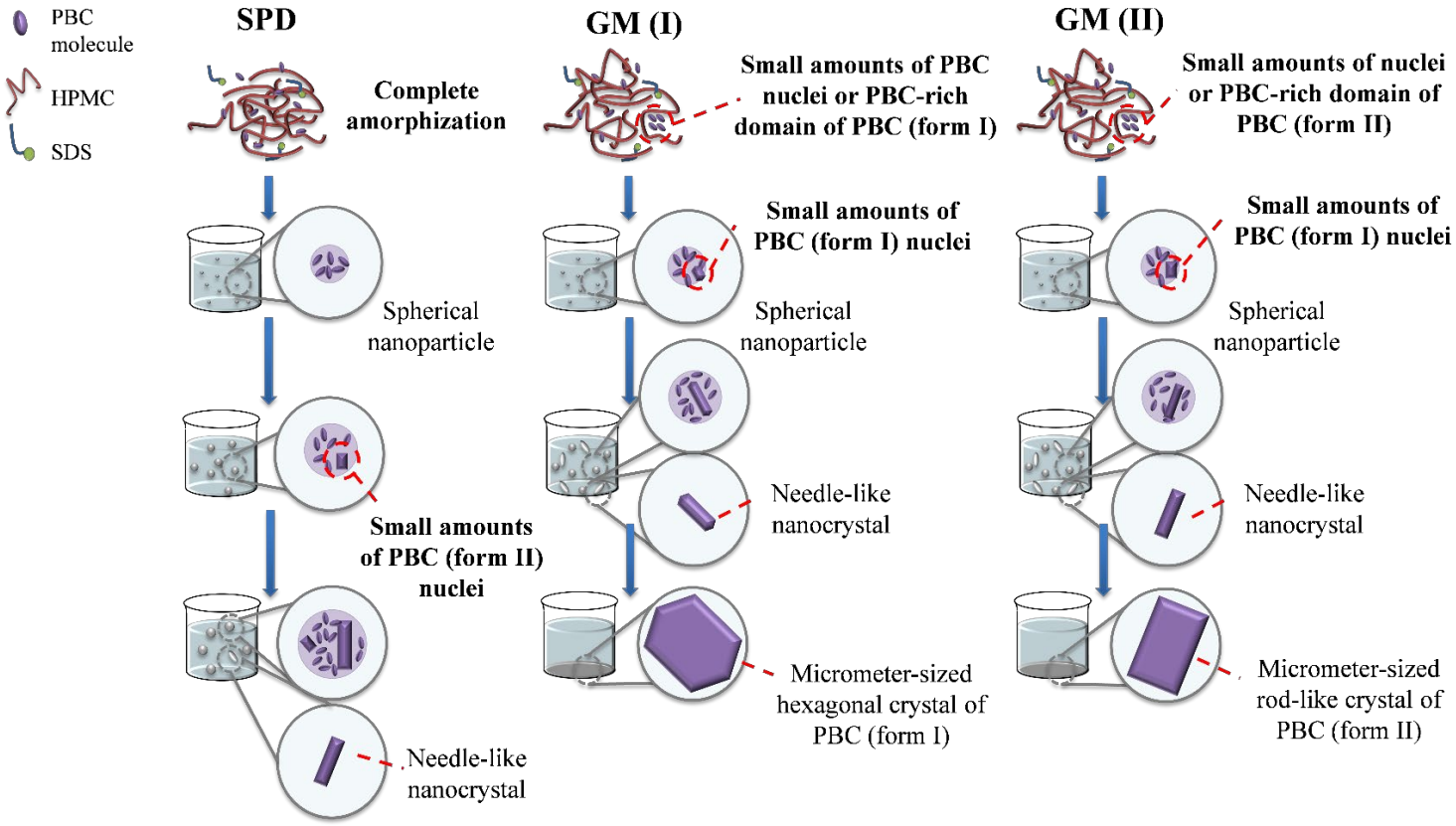

Figure 15. A schematic illustration of the evolution of the PBC nanoparticles after dispersion in water. HPMC and SDS are not shown in the figure after the dispersion into water.

PART II. IMPACT OF COMPOSITION OF TERNARY SOLID DISPERSIONS ON THE FORMATION OF PBC AMORPHOUS DRUG NANOPARTICLES

Characterization of the solid dispersions (SDs)

PXRD measurement

The crystallinities of the PBC/HPMC/SDS ternary SDs were determined using PXRD. All PXRD patterns of the SDs are listed in Figure 16. Most of the SDs, except SD (1:0.5:0), SD (1:0.3:0.5), SD (1:0.3:0.3), and SD (1:0.3:0), did not show PBC crystalline peaks, confirming the amorphous state of the PBC in these SDs. When the weight ratio of PBC/HPMC was less than 1:1, complete amorphization of PBC did not occur after the spray-drying process. The addition of SDS to the composition promoted the amorphization of PBC in the SDs. This could be due to the dilution effect of SDS or the interaction between PBC and HPMC or SDS.

Solid-state ^{13}C NMR spectroscopy

Although PXRD is the mainly-used measurement method for characterizing the crystallinity of drugs in SD, it is difficult to detect the extremely low content (< 2%) of the crystalline phase with this method.[42] As shown in Part I, the trace crystallinity of the drug was sufficient to induce more intensive particle evolution after aqueous dispersion.[43] In order to confirming the molecular state of PBC in SDs, solid-state NMR was utilized as an essential technique for solid-state characterization of SDs in a non-invasive and high-resolution manner. Figures 17 and 18 show the expanded solid-state ^{13}C NMR spectra (from 116 to 160 ppm) and full spectra (from 0 to 180 ppm), respectively. The relatively broad PBC peaks at 123 ppm (C4 peaks) in the spectra

confirmed the amorphous nature of the samples, as revealed by the PXRD measurements. Peak broadening indicated a wide distribution of isotropic chemical shifts resulting from the higher disorder of the amorphous materials.[44] Therefore, based on solid-state NMR spectroscopy, which detects atomic-level information, PBC was amorphized via spray-drying with HPMC and SDS in a series of SDs (1:0.5-4:0.3-2). SD (1:0.3:2) was not included in the measurement because of its extremely low stability, which tended to crystallize within 24 h, even in a low temperature (< 4°C) environment.

Focusing on the hydroxyl carbon peak (C6 peak) of PBC at 155.4 ppm in the ^{13}C solid-state NMR spectrum (Figure 19), it can be found that the hydroxyl carbon peak of PBC in SD (1:0.5:2) and SD (1:0.5:0.3) at 155.4 ppm shifted to 155.9 ppm in SD (1:2:2) and SD (1:2:0.3). Although the peaks appeared to be more sharpened in SD (1:4:2) and SD (1:4:0.3) than in SD (1:2:2) and SD (1:2:0.3), the chemical shift remained constant at 155.9 ppm in SD (1:4:2) and SD (1:4:0.3). Here, a downfield chemical shift occurred as the weight ratio of HPMC increased. It was assumed that there were two molecular states of PBC in the SDs: a lower magnetic field peak resulting from the PBC molecule interacting with HPMC and a higher magnetic field peak derived from its interaction with other PBC molecules. The phenolic hydroxyl group of PBC interacts with the hydroxyl group of HPMC via hydrogen bonding. When the weight ratio of PBC to HPMC was less than 1:2, a larger amount of the PBC molecule was molecularly dispersed in the HPMC matrix and interacted with the HPMC molecule. However, when their weight ratio exceeded 1:2, the PBC molecule could exceed its solubility in the HPMC matrix. Therefore, a molecular interaction was established between PBC-PBC and the PBC-rich domains were generated. Notably, the SDS weight ratio did not affect the chemical shift of the hydroxyl carbon peak of PBC,

suggesting a less observable influence of SDS on the PBC-PBC interaction or PBC-HPMC interaction.

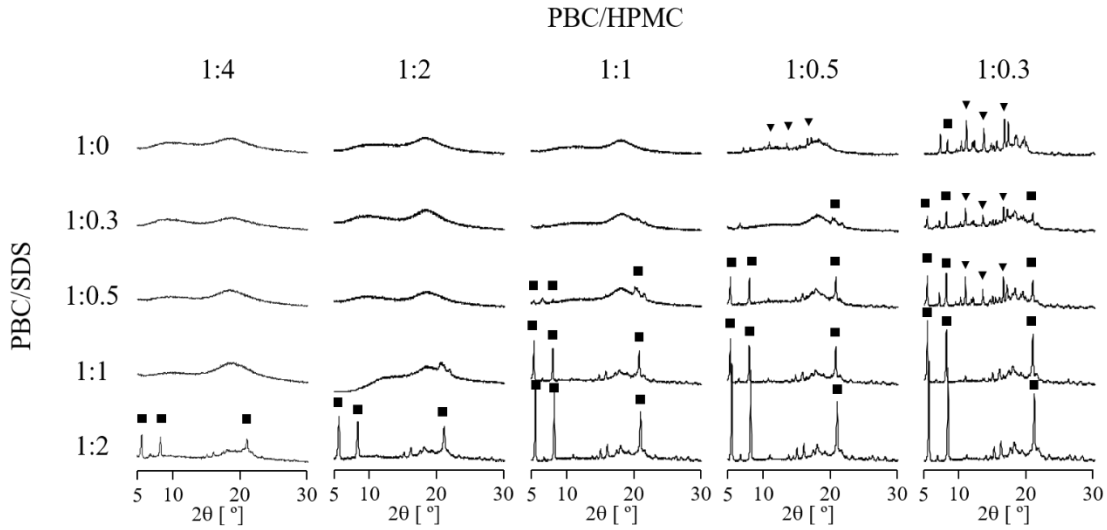

Figure 16. PXRD patterns of SDs prepared with different PBC/HPMC/SDS weight ratios using the spray-drying method. ▼ and ■ represent the characteristic peaks of the PBC crystal and SDS, respectively.

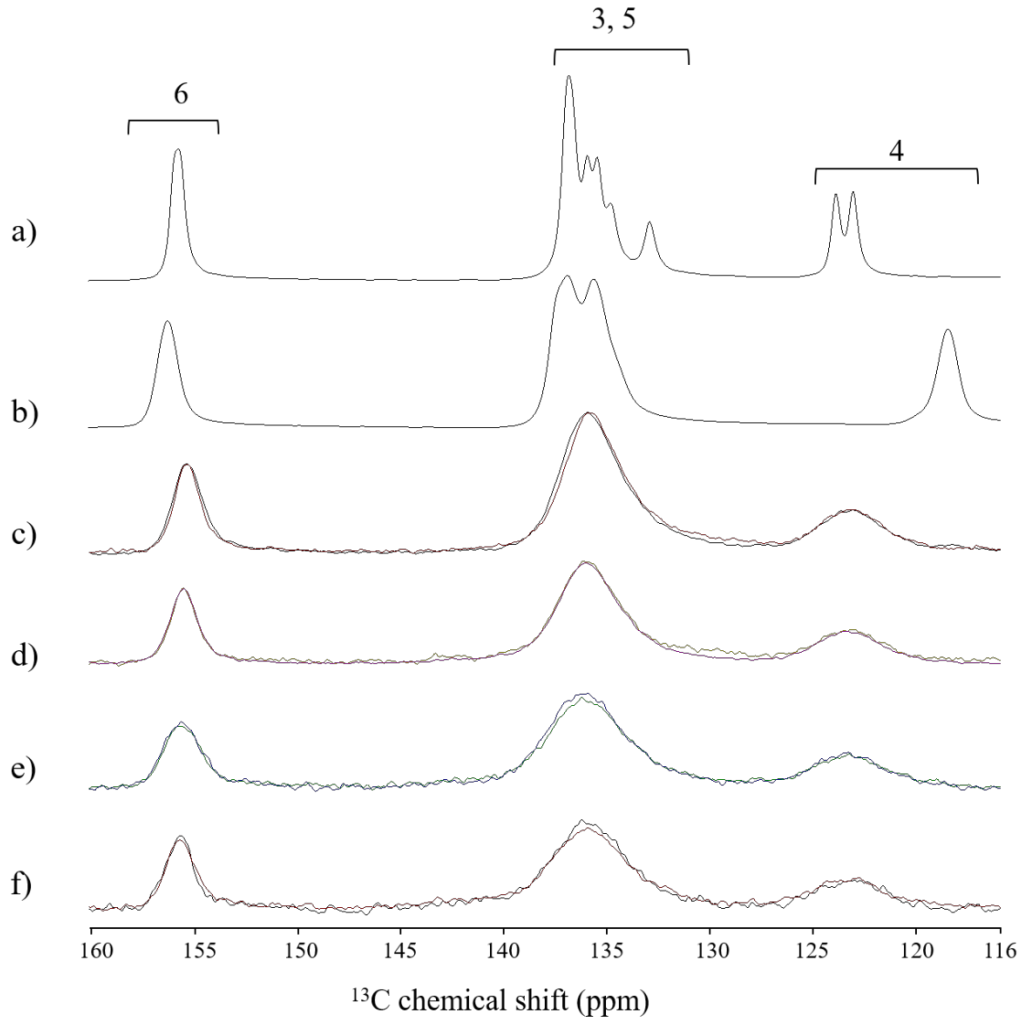

Figure 17. Solid-state ^{13}C NMR spectra (116-160 ppm) of (a) PBC (form I), (b) PBC (form II), (c) SD (1:0.5:0.3) in red and SD (1:0.5:2) in black, (d) SD (1:1:0.3) in purple and SD (1:1:2) in khaki, (e) SD (1:2:0.3) in blue and SD (1:2:2) in green, and (f) SD (1:4:0.3) in red and SD (1:4:2) in black.

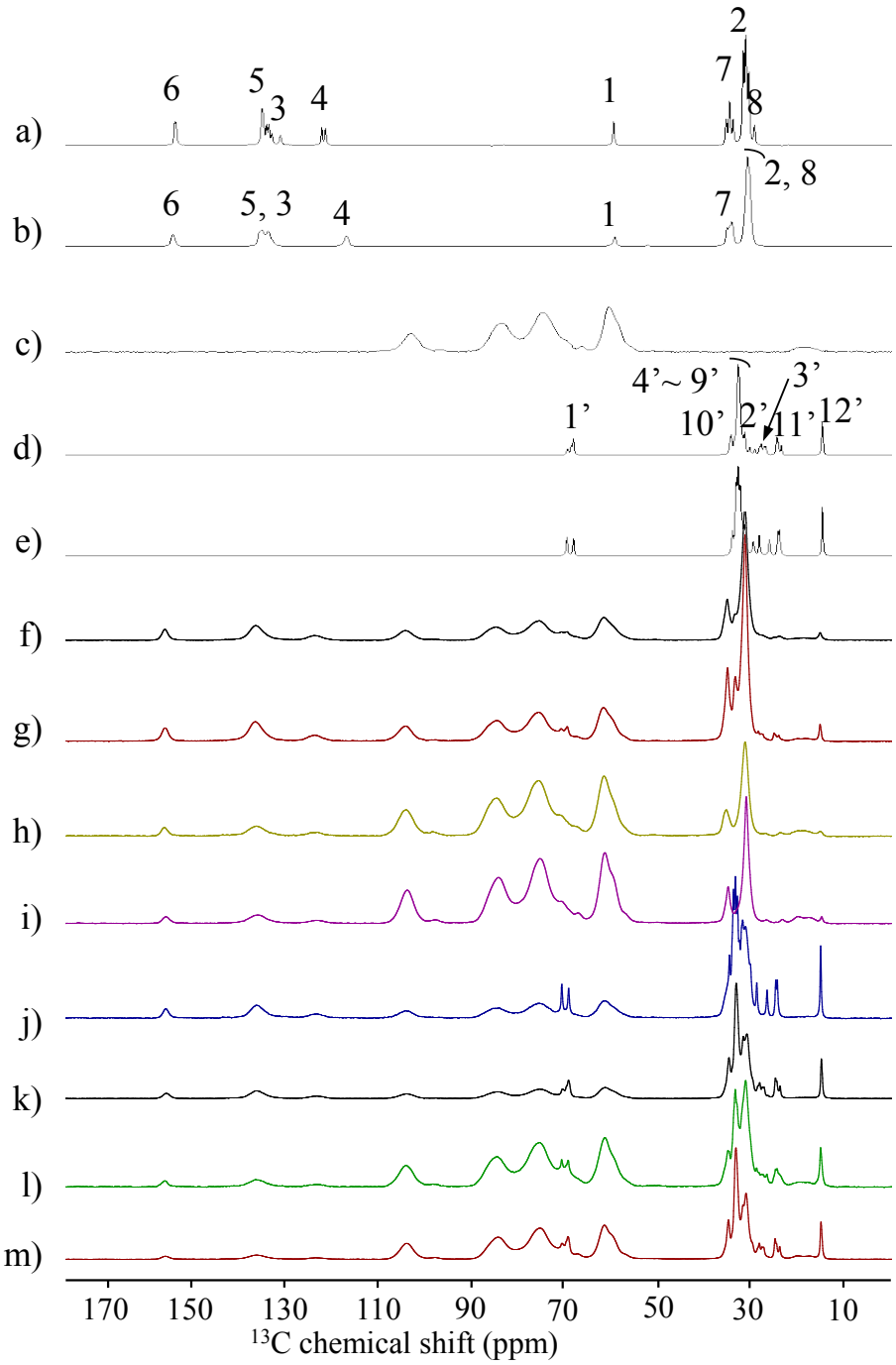

Figure 18. Full-scale solid-state ^{13}C NMR spectra of (a) PBC (form I), (b) PBC (form II), (c) HPMC, (d) SDS, (e) spray-dried SDS, (f) SD (1:0.5:2), (g) SD (1:0.5:0.3), (h) SD (1:1:2), (i) SD (1:1:0.3), (j) SD (1:2:2), (k) SD (1:2:0.3), (l) SD (1:4:2), and (m) SD (1:4:0.3).

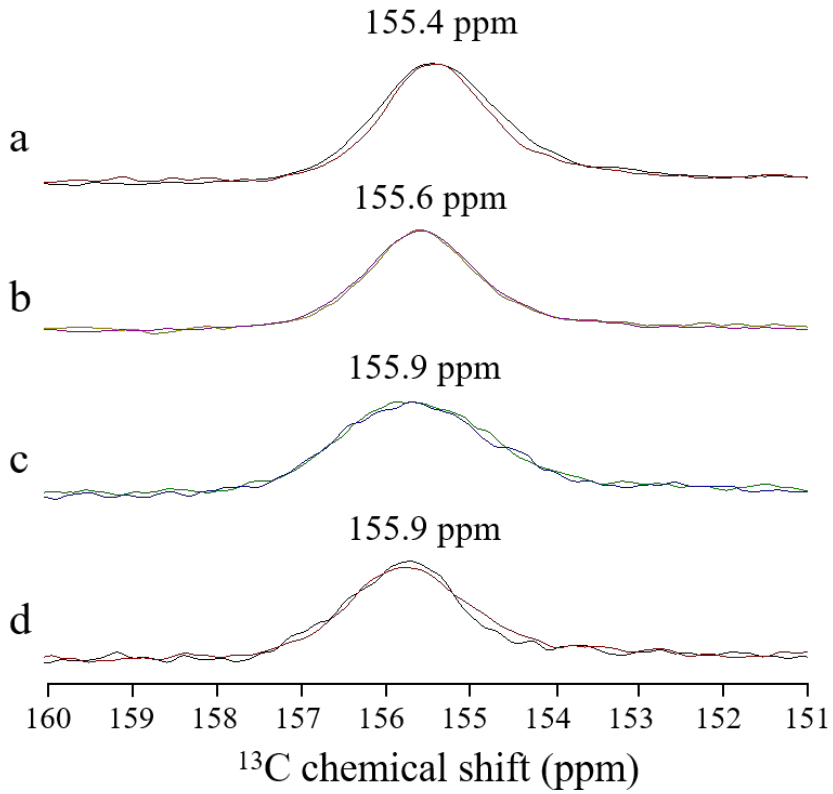

Figure 19. Solid-state ^{13}C NMR spectra (151-160 ppm) of (a) SD (1:0.5:0.3) in red and SD (1:0.5:2) in black, (b) SD (1:1:0.3) in purple and SD (1:1:2) in khaki, (c) SD (1:2:0.3) in blue and SD (1:2:2) in green, and (d) SD (1:4:0.3) in red and SD (1:4:2) in black.

Characterization of the SD suspensions

Particle size distribution.

Twenty PBC/HPMC/SDS SDs prepared with different weight ratios were examined. The MVs of the PBC particles in the SD suspensions were characterized using DLS (Figure 20). The three protocols described in the Methods section were used to prepare the suspension samples. The information captured regarding particle size, including MV, mean number diameter (MN), median particle diameter (d50), standard deviation (S.D.), and polydispersity index (PDI) for each SD suspension sample, are summarized in Table 5. The SD (1:X:0) suspensions were excluded from the results because of their indispensability in distilled water and the HPMC/SDS solutions. For protocol 1 (Figure 20a), the formation of tiny nanoparticles with MVs below 30 nm was observed in suspensions prepared with seven SDs, including SD (1:4:0.3-2), SD (1:2:1-2), and SD (1:1:2). These samples had PDI values less than 0.3. In the pharmaceutical field, a PDI below 0.3 indicates monodispersed drug nanoparticles.[45] The rest of the SD suspensions showed enlarged MVs and PDIs, especially those prepared using SDs with a weight ratio of PBC/SDS and PBC/HPMC lower than 1:0.5 and 1:0.3, respectively. Therefore, high weight ratios of SDS and HPMC in SDs were desirable for producing the drug nanoparticles. In protocol 2, the MVs (Figure 20b) and PDIs (Table 5) were generally smaller than those obtained with protocol 1, especially for the SD (1:2:0.3-0.5), SD (1:1:0.3-1), and SD (1:0.5:0.3-2) suspensions. The pre-dissolved HPMC and SDS helped decrease particle size or inhibit particle evolution (aggregation/agglomeration). Notably, the MVs varied significantly in protocol 2, despite the use of the same input amounts of PBC, HPMC, and SDS in each final SD suspension. The different particle sizes obtained using protocol 2 could be due to (i) the different sizes of the PBC-rich domain in the different SDs and

(ii) the different particle evolution that occurred during or after dispersal in water. No considerable difference in MVs was observed with protocol 3 (Figure 21) relative to protocol 2, despite the use of a total SDS input amount that was 1.5-fold (1.5 mg/mL) greater than that used in protocol 2. According to the result of Part I, almost all of the SDS (>95%) was not included in the nanoparticle; instead, they were freely dissolved in solution in the SD suspension of PBC/HPMC/SDS = 0.5:2.0:1.0 mg/ mL (weight ratio of 1:4:2).[43] The critical micelle concentration and critical aggregation concentration of SDS in the 0.2% HPMC solution at 25 °C were 2.35 mg/mL and 1.56 mg/ml, respectively. Thus, the SDS molecule tended to gather between the interface of the water phase and amorphous drug nanoparticles rather than form the HPMC/SDS complex and micelle.[46] To some extent, the dissolved amount of SDS (1 mg/mL) in the suspension from protocol 2 was sufficient to cover the liquid-liquid interface and inhibit particle evolution via charge repulsion. Therefore, the increased amount of pre-dissolved SDS in protocol 3 compared to that in protocol 2 did not further reduce the MVs of the PBC nanoparticles.

Cryo-TEM measurements.

Cryo-TEM was used to observe the nanometer-scale morphology of the particles in the SD suspensions. Figure 22a-h shows the cryo-TEM images of the SD suspensions prepared using protocol 1. For the SD (1:4:2) and (1:4:0.3) suspensions, the PBC nanoparticles were spherical, with an MN of approximately 20 nm (Figure 22a and b). Their spherical shape suggested a supercooled liquid state of PBC, which was also reported in several studies.[43, 47, 48] The preparation temperature of the SD suspensions in Part II was 25 °C, which is slightly higher than the reported glass transition temperature (T_g) of amorphous PBC (23°C).[41] Considering the T_g of

HPMC (approximately 160 °C) and the T_g confinement effect caused by size reduction and the inclusion of water (T_g = −138 °C) in the nanoparticles, the T_g of the nanoparticles should be lower than 25°C.[49, 50] Collectively, the PBC molecular state in the dispersed nanoparticles should have existed in a supercooled liquid state instead of a glass state. For the other SD suspensions, a clear difference was observed between those prepared with SDs of the same HPMC weight ratio and different SDS amounts. Although 20-nm particles could still be observed in the SD (1:2:2), (1:1:2), and (1:0.5:2) suspensions, the MN gradually increased with decreasing weight ratios of HPMC (Figure 22c, e, and g). However, for the SD (1:2:0.3) and (1:1:0.3) suspensions, in addition to the spherical nanoparticles, some of the particles formed coalesced agglomerates. The agglomeration degree became more aggressive and formed an irregular structure with hundreds of nanometers, depending on the decreasing weight ratio of admixed HPMC in SDs (Figure 22d and f). This finding supported the DLS results (Table 5). The coalesced agglomeration process also revealed the high mobility and supercooled liquid state of the PBC nanoparticles. Finally, some needle-like nanocrystals with particle lengths of more than 200 nm were observed in the SD (1:0.5:0.3) suspension (Figure 22h). These results suggest that the increasing amount of admixed HPMC in the SDs suppressed the primary particle size of the spherical PBC nanoparticles. The primary particle size suggested here was identified as the particle size of discrete PBC nanoparticles at the time point of release from the water-immersed SD. Further, admixed HPMC and SDS significantly suppressed particle evolution (agglomeration and crystallization).

The SD suspensions prepared using protocol 2 were examined to determine the effect of pre-dissolved HPMC and SDS on particle size and evaluate the PBC nanoparticles. The SD (1:4:2), (1:2:2), (1:1:2), and (1:0.5:2) suspensions (Figure 23a, c, e, g) revealed that particle size

increased with decreasing amounts of HPMC in the SDs. The morphologies of the PBC nanoparticles observed in these SD suspensions were identical to those observed when protocol 1 was employed (Figure 22a, c, e, g). Compared to protocol 1, less coalesced agglomerates were observed in the SD (1:2:0.3) and (1;1:0.3) suspensions prepared using protocol 2 (Figure 23d and f). For the SD (1:0.5:0.3) suspension, spherical PBC nanoparticles were mainly observed in the sight field (Figure 23h, indicated by red arrows) compared to the overwhelming number of needle-like nanocrystals observed in their counterparts prepared using protocol 1 (Figure 22h). This result suggests that pre-dissolved HPMC has less influence on further decreasing the particle size of primary amorphous PBC nanoparticles. In comparison, pre-dissolved HPMC and SDS had a significantly positive effect on the suppression of particle evolution and crystallization.

Notably, the sizes of the PBC nanoparticles determined by DLS (Figure 21) were generally larger than those determined with cryo-TEM images (Figures 22 and 23). One reason for this discrepancy is that the particle size obtained using TEM measurement represents the MN while that of DLS represents the MV. However, the MN determined using the DLS measurements (Table 5) was relatively close to that determined with TEM images. Another reason is that TEM provides the actual particle size while DLS yields the hydrodynamic diameter.[51] Only the electron-rich inner core of the particle can be observed in the TEM image. Based on DLS analysis, the polymer or surfactant covering the nanoparticles affects light scattering. Hence, the size measured would reflect both the inner core and shell layer. Therefore, the MN values determined using DLS were still slightly larger than those obtained with the microscopic method.

Statistical analysis of particle diameter versus the roundness.

The scatter plot of particle diameter versus the roundness of the PBC particles in each SD

suspension was generated using cryo-TEM images (Figure 24). At least 300 particles at 30 different locations in each SD suspension were selected and used for the calculations. For protocol 1, the SD (1:4:2) and SD (1:4:0.3) suspensions displayed a similar distribution result (Figure 24a): the plots were concentrated around 15 nm to 20 nm for the diameter and 0.7 to 1 for roundness, suggesting the formation of homogeneous spherical PBC nanoparticles. However, the distribution of plots obtained from the SD (1:2:2) and (1:2:0.3) suspensions became relatively more dispersive, but in different patterns (Figure 24b). For the SD (1:2:2) suspension, nanoparticle collections with relatively larger sizes and high roundness were observed; however, the number was too limited to affect the statistics of the PBC nanoparticle size. In contrast, for the SD (1:2:0.3) suspension, an approximate linear distribution of plots, showing an increase in particle diameter with a decrease in the roundness value, was observed. This negative correlation could be attributed to the formation of irregular coalesced agglomerates, as shown in Figure 22d. The SD (1:1:2) and SD (1:1:0.3) suspensions exhibited similar trends of distribution to the SD (1:2:2) and (1:2:0.3) suspensions, respectively; however, they were more dispersive. This result aligns with the enlarged spherical PBC nanoparticles and the more aggressive particle coalescence observed (Figure 24c). In Figure 24d, the more extended distribution band on the top of the graph, ranging from 0.8-1 in roundness and 15-90 nm in diameter, suggests an increasing amount of larger spherical PBC nanoparticles. A scatter plot of the SD (1:0.5:0.3) suspensions was not generated as almost all observed PBC particles were needle-like nanocrystals, with a length greater than 200 nm and an average roundness smaller than 0.5. The larger size and low roundness value were derived from the needle-shape of the nanocrystal instead of the coalesced agglomerates.

Figure 24e-h shows the scatter plot of particle size versus roundness of the SD suspensions

prepared using protocol 2. Notably, the distribution plots of the SD (1:X:0.3) suspensions prepared using protocol 2 were generally more concentrated than those prepared with protocol 1. When the SD (1:X:2) suspensions prepared with protocols 1 and 2 were plotted, a marked difference was not found. Such finding suggests that pre-dissolved HPMC and SDS can restrain particle agglomeration. In contrast, pre-dissolved HPMC has a lower effect on suppressing the primary particle size of spherical PBC nanoparticles. A general trend can also be observed with protocols 1 and 2: the distribution of the plots for the SD (1:X:2) suspensions was more to the left than those for the SD (1:X:0.3) suspensions, except for the SD (1:4:2) and SD (1:4:0.3) suspensions. Such finding indicates that the minimum particle size of the discrete PBC nanoparticles in the SD (1:X:2) suspensions was relatively smaller than the SD (1:X:0.3) suspensions. The primary particle size of the spherical PBC nanoparticles depended on the amount of admixed SDS in SD rather than the amount of pre-dissolved SDS in water.

PXRD measurements of FDs.

The crystallinity of the PBC nanoparticles in each suspension prepared with a specific weight ratio of PBC/HPMC/SDS (1:X:Y) using protocols 1 and 2 was freeze-dried and examined using PXRD. For the SD suspensions prepared using protocol 1, almost all FDs displayed the amorphous state of PBC, except for five FDs, including FD (1:0.5:0.3-0.5) and FD (1:0.3:0.3-1) (Figure 25a). When the SD suspensions prepared using protocols 1 and 2 were compared, most of the results were found to be the same; however, the PBC in FD (1:0.5:0.5) had an amorphous state instead of the crystalline state mentioned in protocol 1 (Figure 25b). The five SD suspensions that presented the crystalline state of PBC in protocol 1 showed more intense characteristic peaks than their counterparts in protocol 2. Such finding suggests that the pre-dissolved HPMC and SDS

inhibited crystallization and prevented particle evolution of the amorphous PBC nanoparticles.

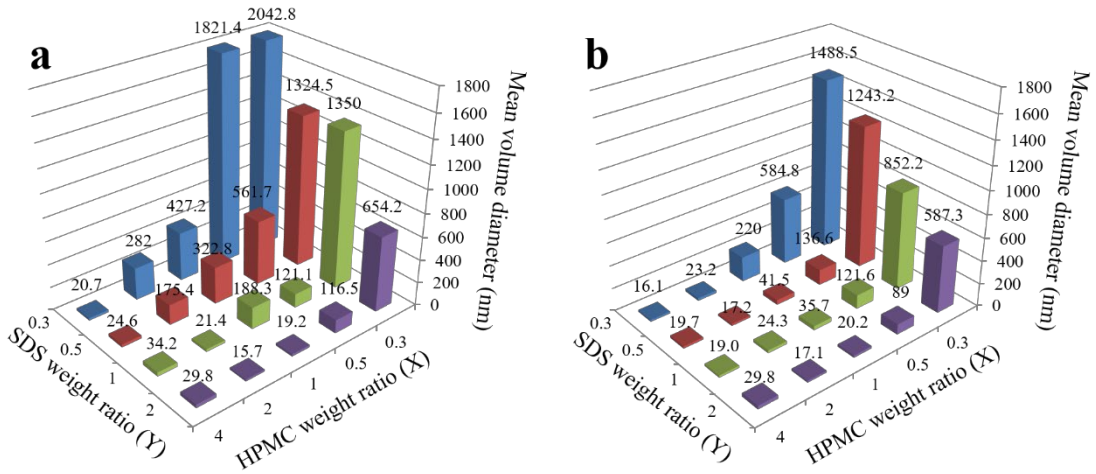

Figure 20. The mean volume diameters (MVs) of the SD suspensions prepared with a specific weight ratio of PBC/HPMC/SDS (1:X:Y) were determined by dynamic light scattering (DLS) using (a) protocol 1 and (b) protocol 2. The X-axis represents the weight ratio of HPMC while the Y-axis represents the weight ratio of SDS. In (a) protocol 1, each SD was directly dispersed in 5 mL of distilled water at a PBC concentration of 0.5 mg/mL. In (b) protocol 2, each SD was dispersed in pre-dissolved HPMC and SDS solution to obtain the input amount of PBC, HPMC, and SDS in a final suspension with a concentration of 0.5:2.0:1.0 mg/mL (weight ratio of 1:4:2).

Table 5. Summarized information of the particle size for each SD (1:X:Y) suspension prepared using protocol 1 (P1) and protocol 2 (P2). The following data are presented: mean volume diameter (MV), mean number diameter (MN), median particle diameter (d50), standard deviation (S.D.), and polydispersity index (PDI) for each SD suspension.

	MV (µm)		MN (µm)		d50 (µm)		S.D. (µm)		PDI	
Samples	P1	P2	P1	P2	P1	P2	P1	P2	P1	P2
SD (1:4:2)	0.0298	-	0.0215	-	0.0273	-	0.0103	-	0.2311	-
SD (1:4:1)	0.0342	0.0194	0.0217	0.0147	0.0257	0.0175	0.0092	0.0061	0.2227	0.1927
SD (1:4:0.5)	0.0246	0.0197	0.0154	0.0150	0.0174	0.0176	0.0061	0.0058	0.1897	0.1717
SD (1:4:0.3)	0.0207	0.0161	0.0143	0.0131	0.0173	0.0154	0.0064	0.0042	0.2203	0.1450
SD (1:2:2)	0.0157	0.0171	0.0122	0.0129	0.0142	0.0153	0.0046	0.0053	0.1702	0.1936
SD (1:2:1)	0.0214	0.0243	0.0153	0.0161	0.0189	0.0203	0.0069	0.0093	0.2284	0.2731
SD (1:2:0.5)	0.1754	0.0172	0.0236	0.0138	0.0343	0.0162	0.0205	0.0049	0.5082	0.1560
SD (1:2:0.3)	0.2820	0.0232	0.0152	0.0171	0.0247	0.0204	0.0268	0.0071	0.7600	0.1970
SD (1:1:2)	0.0192	0.0202	0.0134	0.0149	0.0151	0.0170	0.0052	0.0057	0.1964	0.1829
SD (1:1:1)	0.1883	0.0357	0.0596	0.0178	0.1073	0.0211	0.1233	0.0082	0.8258	0.2344
SD (1:1:0.5)	0.3228	0.0415	0.0827	0.0238	0.1996	0.0291	0.2147	0.0138	1.1046	0.3095
SD (1:1:0.3)	0.4272	0.2200	0.1126	0.0750	0.2432	0.1533	0.2817	0.1371	0.9741	0.5331
SD (1:0.5:2)	0.1165	0.0890	0.0361	0.0461	0.0609	0.0630	0.0807	0.0399	0.7585	0.4090
SD (1:0.5:1)	0.1211	0.1216	0.0282	0.0315	0.0438	0.0509	0.0534	0.0450	0.7378	0.6713
SD (1:0.5:0.5)	0.5617	0.1366	0.0441	0.0467	0.0692	0.0510	0.5343	0.0586	1.0173	0.6266
SD (1:0.5:0.3)	1.8214	0.5848	0.0474	0.1922	1.1975	0.3256	1.8864	0.3870	4.2111	0.7567
SD (1:0.3:2)	0.6542	0.5873	0.1085	0.1041	0.4693	0.5464	0.5261	0.4346	1.8677	1.8678
SD (1:0.3:1)	1.3500	0.8522	0.1286	0.1628	0.7723	0.5671	0.9762	0.5433	3.6394	1.3588
SD (1:0.3:0.5)	1.3245	1.2432	0.5433	0.2704	1.3513	1.0952	0.6315	0.8419	1.7745	1.5689
SD (1:0.3:0.3)	2.0428	1.4885	0.4339	0.2657	1.9979	1.2933	0.8944	0.8052	2.0470	2.1099

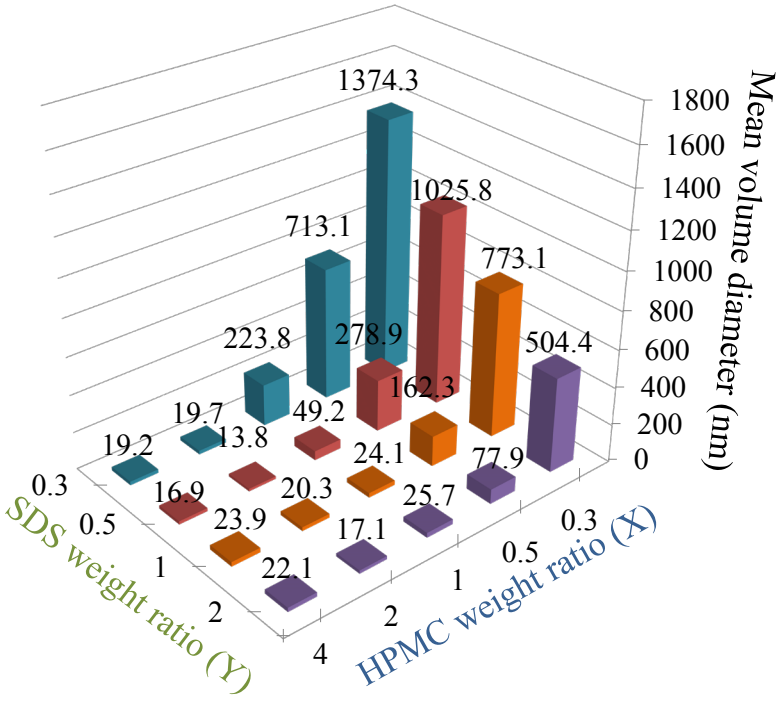

Figure 21. The mean volume diameters (MVs) of the SD suspensions prepared with a specific weight ratio of PBC/HPMC/SDS (1:X:Y) were determined by dynamic light scattering (DLS) using protocol 3. The X axis indicates the weight ratio of HPMC, while the Y axis represents the weight ratio of SDS. In protocol 3, each SD was dispersed in pre-dissolved HPMC and SDS solution to yield a final suspension concentration of 0.5:2.0:2.0 mg/mL (weight ratio of 1:4:3) using PBC:HPMC:SDS.

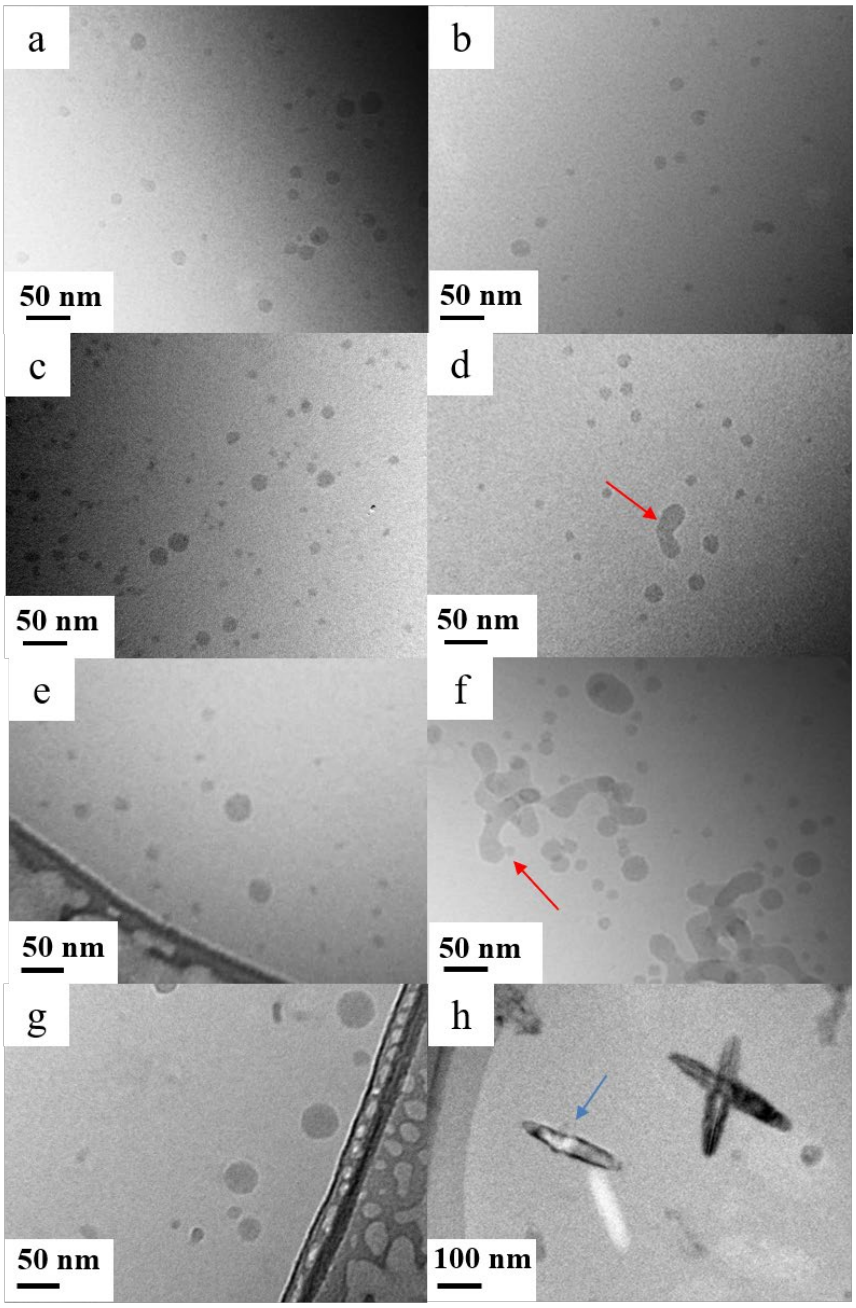

Figure 22. Cryo-TEM images of the (a) SD (1:4:2), (b) SD (1:4:0.3), (c) SD (1:2:2), (d) SD (1:2:0.3), (e) SD (1:1:2), (f) SD (1:1:0.3), (g) SD (1:0.5:2), and (h) SD (1:0.5:0.3) suspensions prepared using protocol 1. The red arrows in (d) and (f) indicate coalescence structure. The cyan arrows in (h) indicate needle-like PBC nanocrystals.

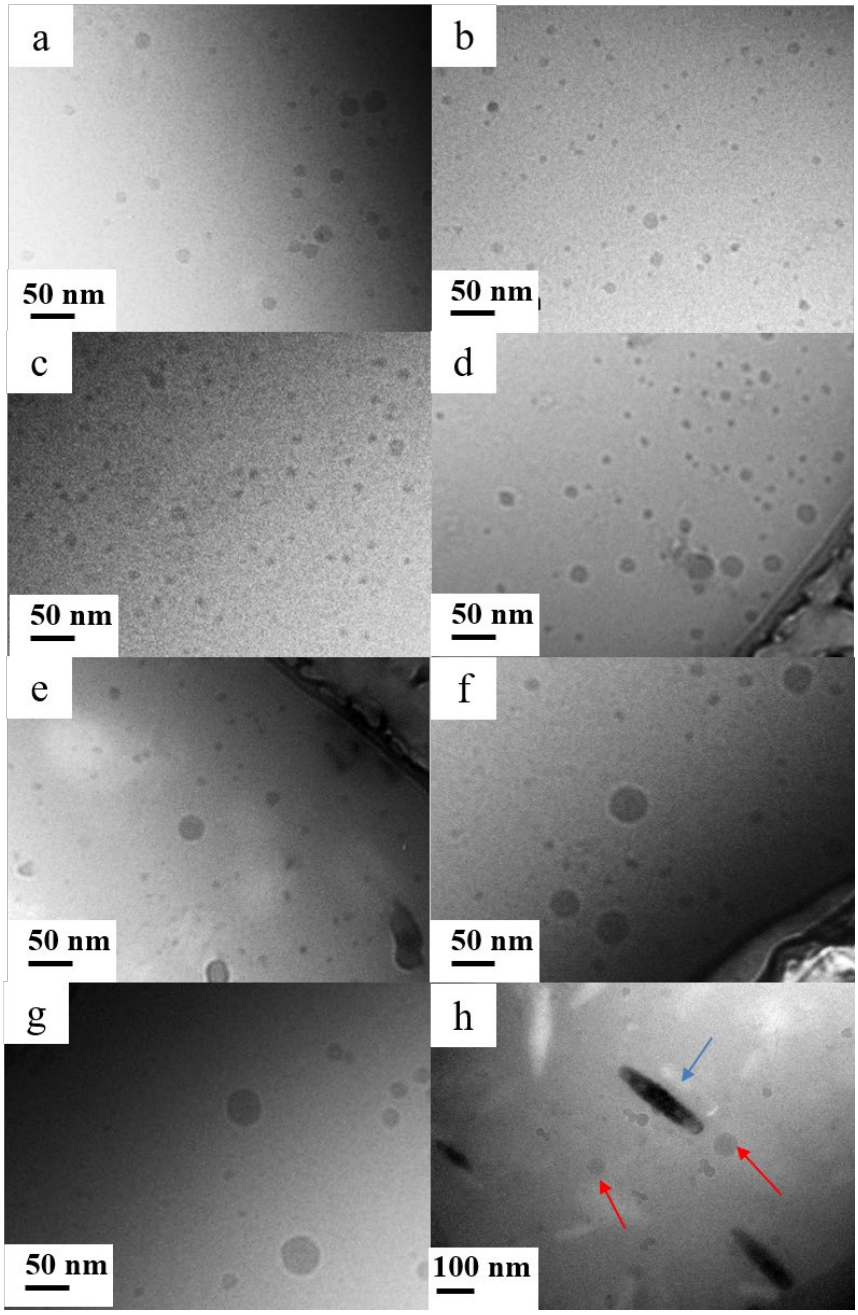

Figure 23. Cryo-TEM images of the (a) SD (1:4:2), (b) SD (1:4:0.3), (c) SD (1:2:2), (d) SD (1:2:0.3), (e) SD (1:1:2), (f) SD (1:1:0.3), (g) SD (1:0.5:2), and (h) SD (1:0.5:0.3) suspensions prepared using protocol 2. The cyan and red arrows in (h) indicate needle-like PBC nanocrystals and spherical PBC amorphous nanoparticles, respectively.

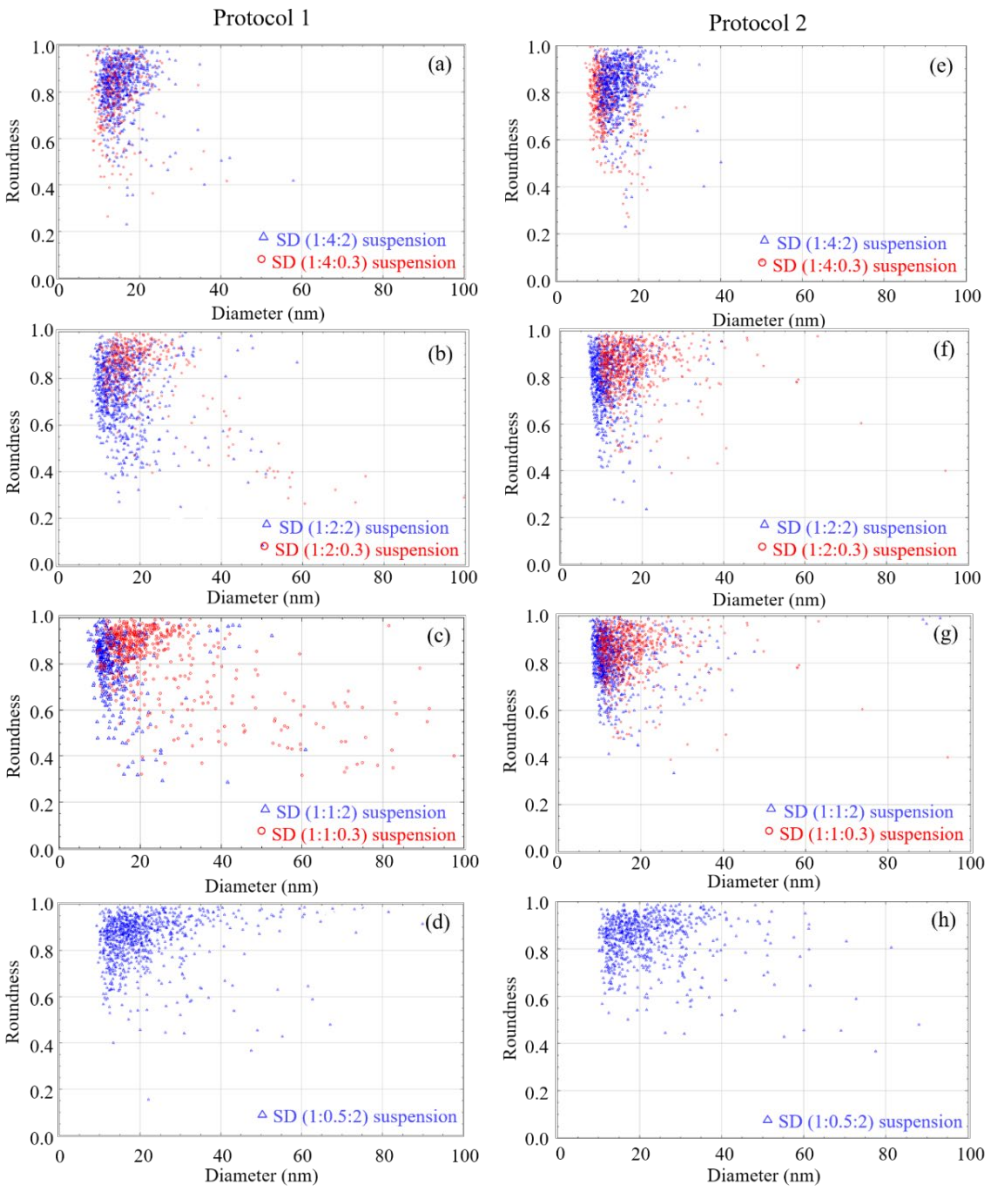

Figure 24. Scatter plots of the particle diameter versus the roundness of the PBC nanoparticles in (a) SD (1:4:2) and SD (1:4:0.3), (b) SD (1:2:2) and SD (1:2:0.3), (c) SD (1:1:2) and SD (1:1:0.3), and (d) SD (1:0.5:2) and SD (1:0.5:0.3) suspensions prepared using (left) protocol 1. Their counterparts prepared using (right) protocol 2 are shown in (e)-(h). For each SD suspension, more than 300 particles were analyzed. The particle diameter is defined as the longest distance between any two points along the selection boundary of the particle. Roundness with a value of 1.0 indicates a perfect circle. As the value approaches 0.0, this indicates an increasingly elongated shape.

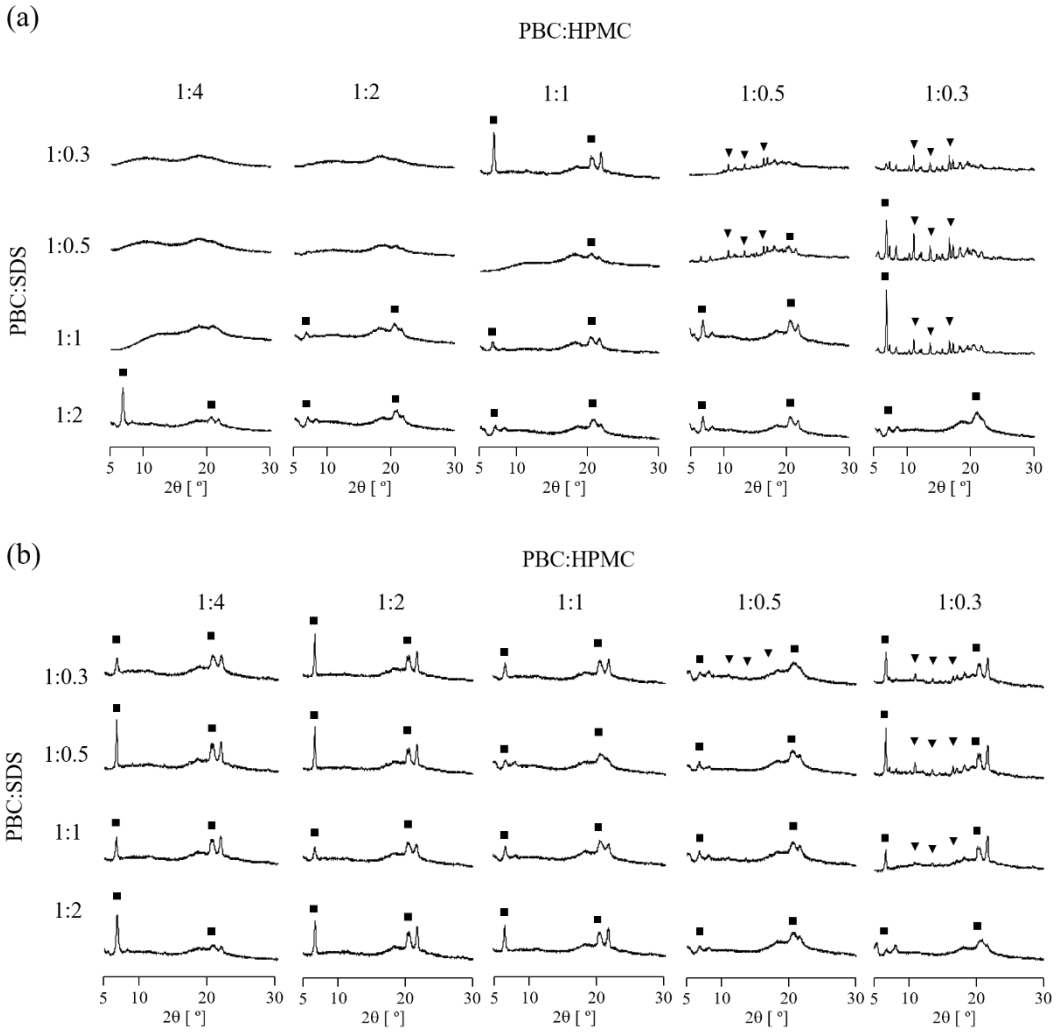

Figure 25. PXRD patterns of the freeze-dried SD suspensions prepared using different weight ratios of PBC/HPMC/SDS via (a) protocol 1 and (b) protocol 2. ▼ and ■ represent the characteristic peaks of the PBC crystal and SDS, respectively.

Discussion of the effect of HPMC and SDS on the formation of amorphous PBC nanoparticles

Herein, the influence of polymers and surfactants in SDs on the nanostructure of SDs and the particle morphology and evolution of the resulting amorphous drug nanoparticles was discussed. Based on the results described above, the aqueous dispersion process was divided into three stages: Ⅰ) before dispersion, Ⅱ) water immersion into SDs, and Ⅲ) complete release from SDs (Figure 26).

In the first stage (Figure 26 Ⅰ), HPMC plays the main role in determining the molecular state of SDs. The different weight ratios of HPMC could lead to different PBC-rich domains within SDs. Li et al. reported the topographical features of telaprevir–polymer systems using different drug-to-polymer ratios. They found that as the polymer weight ratio decreased, the drug-rich domains in the height image became more irregular in shape and less uniform in size.[52] The result of solid-state ^{13}C NMR measurement evidenced this proposal. In contrast, SDS was demonstrated to show less effect on the molecular state of PBC in the SDs.

For the second stage of water immersion (Figure 26 Ⅱ), the SDs with different weight ratios of admixed HPMC and SDS could lead to the different evolution of PBC-rich domains within SDs. To simplify the discussion, It is hypothesized that phase-separated SD consists of only two phases, a drug-rich phase and a polymer-rich phase, where the former phase forms discrete domains embedded in the latter phase. When water is immersed in SD, the polymer-rich phase undergoes amorphous–amorphous phase separation and evolves into drug-rich domains with sizes of several nanometers. Meanwhile, the drug-rich phases become more irregular in shape and size, depending on the decreasing weight ratio of the polymer. The drug-rich phase disintegrates if these regions

are not interconnected or undergo small-scale agglomeration when they are located too close to each other. Despite the simplification we discussed above, phase-separated SD systems in the actual case should be more complicated because of the formation of multiple phases or the interconnectivity of the drug-rich regions. By comparing the case with different HPMC weight ratios, HPMC affected the size of the drug-rich domain and played a crucial role in inhibiting the recrystallization of amorphous PBC caused by water absorption. The low weight ratio of admixed HPMC induces the formation of the PBC nucleus during water immersion. By comparing the case with the different SDS weight ratios, a sufficient amount of admixed SDS could efficiently suppress the size increase of PBC-rich domains produced by coalescence.

At the third stage of complete release of SDs (Figure 26Ⅲ), the local supersaturation and enhanced mobility of PBC due to rapid release into the aqueous phase could make the drug-rich domain undergo rapid Ostwald ripening or coalesced agglomeration. Thus, the different degrees of drug-rich domains forming in the second stage led to different particle sizes of the amorphous drug nanoparticles. The drug-rich domains with sizes of several nanometers evolved from the polymer-rich phase in SDs are released into the bulk solution as drug amorphous nanoparticles with a size of approximately 20 nm (Figure 26a–e, h). Therefore, a plot collection of small diameters (approximately 20 nm) was exhibited in all suspension samples (Figure 24). The drug-rich phase in SDs could, however, result in relatively larger amorphous drug nanoparticles (20–80 nm) after aqueous dispersion (Figure 26c–e, h).

In this stage, the HPMC was evidenced to affect particle evolution (agglomeration and crystallization). Maghsoodi et al. reported that the HPMC had an outstanding capability of suppressing the agglomeration of celecoxib nanoparticles, [53] which supported the observation in

Figure 24. As HPMC contains hydrophobic substituents (methoxyl group), it can be adsorbed onto the interface of the hydrophobic drug nanoparticles and lower the interfacial tension due to its surface activity. In addition, the HPMC molecules were also distributed in the core of amorphous PBC nanoparticles and in the bulk aqueous phase. Previously, the concentrations of HPMC in the amorphous PBC nanoparticles of SD [(1:4:2) and (1:1.75:1.25)] suspensions were quantified using solution-state ^{1}H NMR measurements. The results suggested that the PBC/HPMC ratio in the SD (1:1.75:1.25) suspension was 1:0.4, which was higher than the 1:0.55 detected in the SD (1:4:2) suspension. Accordingly, the lower weight ratio of the HPMC admixed in SD was related to the lower concentration of HPMC in the amorphous drug nanoparticles or on the interface of particles. Moreover, most of the HPMC should freely dissolve in the bulk solution phase.[43, 47] The HPMC molecules located in the core, on the interface of amorphous PBC nanoparticles, and in the bulk aqueous phase should possess a crystallization inhibitory effect. According to classical nucleation theory, a higher absolute concentration and a lower magnitude of interfacial tension between the nascent crystal and the solution could result in a relatively higher nucleation rate.[54] Thus, crystallization is favored in the core or on the interface of amorphous PBC nanoparticles instead of in the bulk aqueous phase. Because the solute concentration in the nanoparticles should be substantially higher, the interfacial tension would be lower between a nascent crystal of PBC and its amorphous nanoparticles than between the same crystal and a dilute aqueous solution.[39] Therefore, the HPMC localized in the core of the nanoparticles and at the interface play crucial roles in preventing the nanoparticles from undergoing PBC crystallization. The HPMC inside amorphous PBC nanoparticles could decrease the enhanced mobility of the PBC molecules via water sorption[55] and stabilize the PBC molecules via interaction.[56] While, the HPMC on the

interface of particles could also inhibit the nucleation process by occupying the high-energy interface.[57] The crystallization of PBC in the bulk aqueous phase could be prevented via interaction with dissolved HPMC through noncovalent interactions.[56] Therefore, the PBC nanoparticles in the SD (1:0.5:0.3–0.5) suspensions prepared using protocol 1 had a crystalline state (Figure 25a) due to the lack of HPMC, which would prevent crystallization in all three locations. Thus, the lack of admixed HPMC induced the formation of the PBC nucleus during the water immersion process and further accelerated the crystal growth resulting in the hundreds of nanometer-sized PBC nanocrystal (Figure 26f). In protocol 2, the pre-dissolved HPMC replenished the amount of HPMC in the bulk aqueous phase. As a result, it could suppress crystallization both in the bulk aqueous phase and the interface of the nanoparticles. However, the PBC nucleus existed in water-immersed SDs could still undergo crystal growth though HPMC partly inhibited this process by covering the interface of PBC nucleus (Figure 26g).

When the effect of SDS on the formation of amorphous PBC nanoparticles in the third stage was examined, it was found that the addition of SDS to the formulation facilitated particle formation and suppressed particle-particle interactions. Dave et al. reported that SDS incorporated in SD has a prominent effect on improving drug dissolution.[58] Further, as SDS concentration increased in the SD formulation, the dissolution rate of the drug increased. Similarly, in this study, the binary SDs that did not contain SDS were difficult to disperse in the aqueous solution, suggesting that the addition of SDS affected the fast release and disintegration of ternary SDs. When amorphous drug nanoparticles are entirely released into the aqueous phase, less particle evolution occurs because of the numerous SDS covering the interface of the nanoparticle. However, when the SDS admixed in SDs was initially insufficient to inhibit the drug-rich domain

coalescence, the particle evolution (agglomeration and crystallization) after dispersion could violently proceed because of increased mobility and high interface tension (Figure 26c, e, f, h). In such a case, the addition of SDS (pre-dissolved SDS) could, to some extent, act as remediation. The enlarged amorphous drug nanoparticles resulting from the coalescence of PBC-rich domains were significantly suppressed by the covering of the interface by the surfactant. However, their sizes were still larger than those prepared by a high weight ratio of admixed SDS (Figure 26d, g).

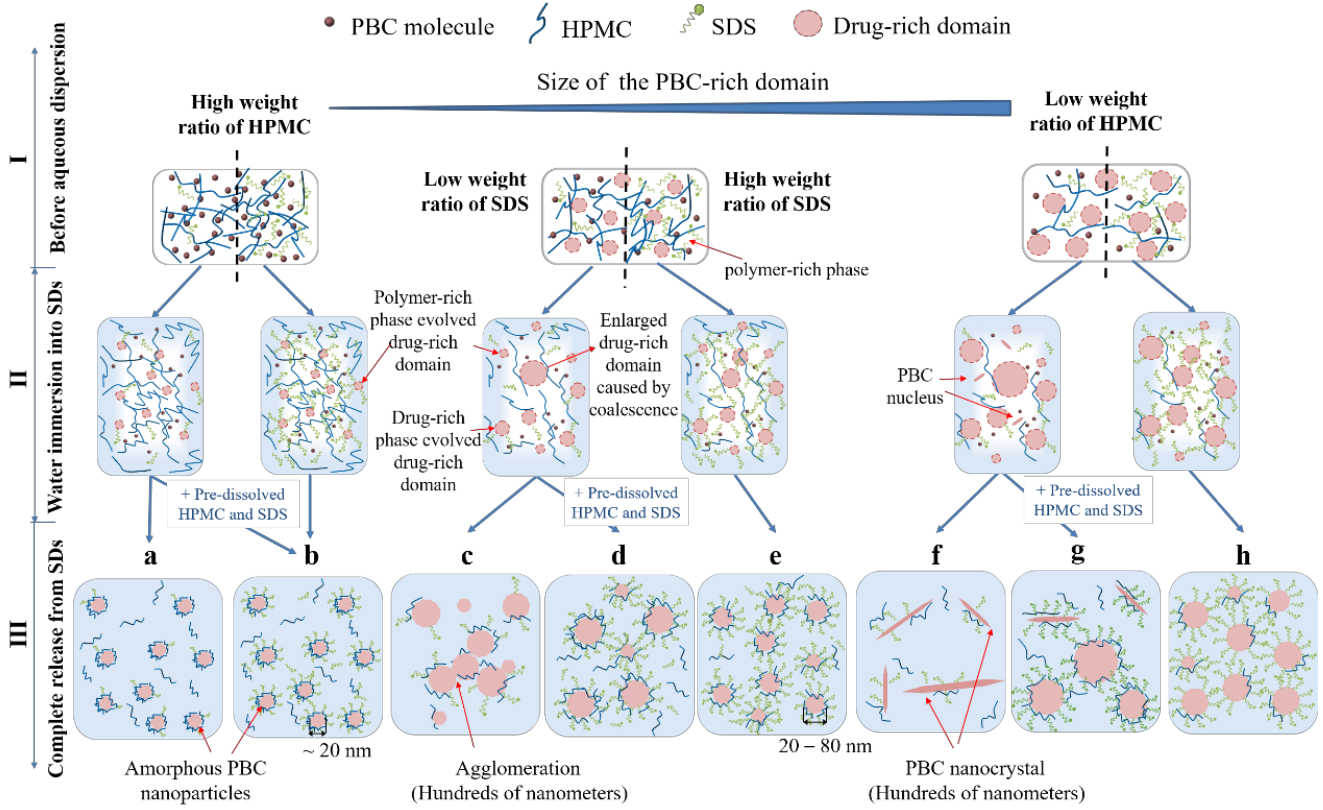

Figure 26. Scheme of the effect of HPMC and SDS on the molecular state of SD Ⅰ) before aqueous dispersion, Ⅱ) during water immersion into SDs, and Ⅲ) the complete release of amorphous PBC nanoparticles from SDs after aqueous dispersion. **a–h** in the scheme exhibited the varied morphology of PBC particles formed after aqueous dispersion of ternary SDs of different weight ratio of HPMC and SDS. HPMC included in the core of PBC particles after aqueous dispersion is not shown.

CONCLUSIONS

The investigations were carried out to elucidate I) the preparation methods and II) the composition of probucol (PBC)/hypromellose (HPMC)/sodium dodecyl sulfate (SDS) ternary solid dispersion (SD) on the stability and formation of amorphous PBC nanoparticles after aqueous dispersion.

In Part I, the mechanisms influencing the physical instability of amorphous PBC nanoparticles formed by the aqueous dispersion of PBC/HPMC/SDS ternary SDs prepared by spray-drying and co-grinding methods were elucidated. The results obtained are concluded as follows:

1. The amorphization of PBC in the spray-dried sample (SPD) and ground mixtures (GMs) was confirmed using powder X-ray diffraction and solid-state ^{13}C nuclear magnetic resonance (NMR) spectroscopy. Additionally, differential scanning calorimetry showed that relatively small amounts of PBC nuclei or PBC-rich domains could remain in both GMs.
2. The results of DLS and cryogenic transmission electron microscopy (cryo-TEM) measurements showed that SPD and GM provided the same spherical PBC nanoparticles smaller than 30 nm just after aqueous dispersion but different particle evolution during storage. For the SPD suspension, the spherical shapes of the PBC nanoparticles were kept during storage, but the size gradually increased. In contrast, the PBC nanoparticles in GM suspension evolved through three morphological changes: gradual size increase of spherical nanoparticles, the formation of needle-like nanocrystals, and micrometer-sized crystals.
3. The force-distance curves measurement of freshly prepared PBC nanoparticles in the GM

suspension showed a steeper slope in the approach process than those in the SPD suspension. The PBC nanoparticles in the GM suspension had a stiffer and more rigid structure than those in the SPD suspension, suggesting that a small amount of PBC crystal phase was generated in the spherical nanoparticles in the GM suspension.

Conclusively, the relation between the molecular states of the drug in SDs depending on the preparation methods and the physical stability of the amorphous drug nanoparticles was revealed. The differences in the trace crystallinity of SDs could strongly affect the physical stability of amorphous drug nanoparticles on storage. The findings confirmed the importance of comprehensive studies to observe the molecular states before and after the dispersion of the SD in water

In Part II, twenty kinds of SDs prepared with different weight ratios of PBC/HPMC/SDS were prepared and investigated for elucidating the impact of the composition of ternary SD on the formation of amorphous PBC nanoparticles formed after aqueous dispersion. Besides, the effect of both admixed and pre-dissolved HPMC and SDS on the three stages of the aqueous dispersion of SDs: before aqueous dispersion, during water immersion in SDs, and complete release from SDs, were discussed.

1. The morphological variations of the PBC nanoparticles in the different SD suspensions were observed by cryo-TEM and the statistical analysis of particle size versus roundness.
    - The increasing amount of admixed HPMC in SDs reduced the primary particle size of the amorphous PBC nanoparticles. Although the pre-dissolved HPMC had less impact on the primary particle size, it inhibited the particle agglomeration

and recrystallization of amorphous PBC nanoparticles.

- Sufficient admixed SDS suppressed the size enhancement of the PBC-rich domains during water immersion and nanoparticle evolution (agglomeration and crystallization) after aqueous dispersion. The pre-dissolved SDS could restrain the agglomeration of amorphous PBC nanoparticles, ultimately forming hundreds of irregular nanometer-order structures. However, the size increase during water immersion is hard to inhibit.

2. Based on ^{13}C NMR measurement, although the amorphous state of the drug was confirmed in all the selected SDs, the decreasing admixed amount of HPMC in SDs leads to a decrease in the miscibility of PBC and HPMC. The size of the PBC-rich domains increased, and the varied size of the PBC-rich domains in the SDs further provided the different primary sizes of the discrete amorphous PBC nanoparticles after aqueous dispersion,

Concisely, the comprehensive studies to evaluate the molecular states of SD: trace crystallinity of the drug, phase separation-induced drug-rich phase, or homogeneous dispersion of a drug in a polymer matrix, is required for manufacturing the tiny and stable formulation of SD-based amorphous drug nanoparticles. In addition, surfactant exhibited outstanding performance in improving dispersibility and suppressing particle evolution (agglomeration and crystallization) in the suspended state, ultimately confirming the usefulness and necessity of adding surfactants in SDs to the fabrication of drug nanoparticle formulations.

FUTURE DIRECTIONS

Throughout this dissertation, the molecular state of drug in solid dispersion (SD) was emphasized for investigating its effect on the formation of amorphous drug nanoparticles via aqueous dispersion of SD. In this study, it has been clarified that the weight ratio of drug to polymer could affect the miscibility of SD resulting in the formation and varied sizes of drug-rich domains. The results confirmed the importance of the phase homogeneity of SD on the formation of tiny and stable amorphous nanoparticles. The various other factors, such as different drug/polymer systems, moisture, temperature, and etc., which can potentially influence the phase homogeneity of SD, should be taken into account in the future studies.

For the different drug/polymer model systems, the selection of polymer is crucial, which should both fulfill the phase homogeneity of SD with a high drug loading as possible and an efficient stabilization effect for amorphous drug nanoparticles in the suspension state. For the SD, the high solubility of drug in polymer matrix is desirable. Theoretically, the miscibility behavior of the blend of two stable amorphous components can be typically described by the will-known Flory-Huggins theory.[59, 60] The application of Flory-Huggins theory has been shown useful while with limitations as well.[61, 62] Experimentally, many techniques, such as X-ray diffraction, differential scanning calorimetry, solid-state nuclear magnetic resonance measurement, and etc. has been used to determine the miscibility of SDs at molecular level and the mechanistic investigation of the drug-polymer interactions. However, these methods are focusing on the static mixing state of the system but not the thermodynamic nature, equilibrium miscibility, of the SDs. This leads to numerous preparation and examination of the SDs with different polymers and drug

loadings in the practical industrial development, resulting in the largely trial and error of the development of SD. Hence, more fundamental understanding and novel technique are highly desirable to reveal the destabilization mechanism of amorphous SDs and then some industrial standards may be established for SD development. On the other hand, the effect of polymer after aqueous dispersion of SD is also important. In Part I, it is evidenced that a part of polymer could embedded in or cover on the amorphous drug nanoparticles. These two parts of polymer are both indispensable, which could restrict molecular mobility and prevent nucleation and growth of the nanoparticles, respectively. It has been reported that the hydrophobic-modified polymer could localize in the interior of drug particle due to the hydrophobic interaction between drug and polymer, which both efficiently inhibited the crystallization and particle size increase.[39] The charged polymer, as well as charged surfactant, could cover the interface of drug particles and prevent the particle size increase by charge repulsion. The question is that what kinds of polymer could both fulfill the high miscibility with drug in SD and work in both location of amorphous drug nanoparticles after aqueous dispersion at once. If it is hard to satisfy these needs with one kind of polymer, is it possible to apply the co-polymer system or modified polymer to fulfill this requirement.

The addition of surfactant in SD is a new emerging field, which needs more scientific investigations. It has been evidenced that the ternary SD is superior to that binary system dispersed in surfactant solution for the formation of amorphous drug nanoparticles. After aqueous dispersion, the surfactant could almost dissolve in aqueous phase, thereby its location and molecular state is predictable. However, the molecular state of surfactant before aqueous dispersion and the influence on the phase homogeneity, physical stability, and hygroscopicity of

SD are still unclear. Moreover, it would be interesting to develop any correlation between the phase homogeneity and dissolution characteristics. The study on drug/polymer/surfactant ternary SD could be extended on other model drugs and polymer combinations. Along those lines, studying surfactants as a part of SD could open new avenues for research.

ACKNOWLEDGEMENTS

The greatest person, to whom I have to mention first of all, is my graduate supervisor. Professor Dr. Kunikazu Moribe, for his kindness and indefinite help given to me. A million of words may not be fulfilled my deepest gratitude I would like to express. Herein, I have just mentioned my thankfulness and appreciation concisely for his keen helpful suggestion and instruction and understanding of any problems. I would like to thank for his constructive criticism and invaluable assistance during my work. Without his understanding, encouragement and kind cooperation, I believe that my research work would have never been succeeded. I owe his endless thanks.

I would like to express my sincere gratitude and thankfulness to Associate Professor Dr. Kenjirou Higashi and Assistant Professor Dr. Keisuke Ueda for their helpful discussion, constructive criticism, invaluable advice, and academic experience throughout my research work in Japan. They also give me warm hospitality and cordial kindness that I will be indebted to them forever. Without their kindful help, I would lose during my research work.

I wish to appreciate Dr. Kohsaku Kawakami at National Institute for Material Science for his scientific advice and support in MDSC measurement.

I also thank Daiichi Sankyo Co., Ltd. for the kind offer of probucol and Shin-Etsu Chemical Co., Ltd. for gifting HPMC.

I appreciate the warm hospitality given by the members of the Laboratory of Pharmaceutical Technology and my parents. Without their supports and encouragement, both the experimental and sentimental aspect, my study in Japan would be more tough and deserted. The person whom I would like to mention namely is my senior, Mr. Hiroaki Katai, for his helpful previous study and

experimental data. This study is partly based on his experiment and hard to accomplish without his contribution.

REFERENCE

1. Kawabata, Y.; Wada, K.; Nakatani, M.; Yamada, S.; Onoue, S., Formulation design for poorly water-soluble drugs based on biopharmaceutics classification system: basic approaches and practical applications. *Int. J. Pharm.* **2011,** *420* (1), 1-10.

2. Williams, H. D.; Trevaskis, N. L.; Charman, S. A.; Shanker, R. M.; Charman, W. N.; Pouton, C. W.; Porter, C. J., Strategies to address low drug solubility in discovery and development. *Pharmacol. Rev.* **2013,** *65* (1), 315-499.

3. Loftsson, T.; Brewster, M. E., Pharmaceutical applications of cyclodextrins: basic science and product development. *J. Pharm. Pharmacol.* **2010,** *62* (11), 1607-1621.

4. Taylor, L. S.; Zhang, G. G. Z., Physical chemistry of supersaturated solutions and implications for oral absorption. *Adv. Drug Deliv. Rev.* **2016,** *101*, 122-142.

5. Blagden, N.; de Matas, M.; Gavan, P. T.; York, P., Crystal engineering of active pharmaceutical ingredients to improve solubility and dissolution rates. *Adv. Drug Deliv. Rev.* **2007,** *59* (7), 617-630.

6. Serajuddin, A. T., Salt formation to improve drug solubility. *Adv. Drug Deliv. Rev.* **2007,** *59* (7), 603-616.

7. Nagarajan, R.; Ruckenstein, E., Theory of surfactant self-assembly - a predictive molecular thermodynamic approach. *Langmuir* **1991,** *7* (12), 2934-2969.

8. Morrison, P. W.; Connon, C. J.; Khutoryanskiy, V. V., Cyclodextrin-mediated enhancement of riboflavin solubility and corneal permeability. *Mol. Pharmacuetics*. **2013,** *10* (2), 756-762.

9. Loftsson, T.; Brewster, M. E., Pharmaceutical applications of cyclodextrins. 1. Drug solubilization and stabilization. *J. Pharm. Sci.* **1996,** *85* (10), 1017-1025.

10. Rajewski, R. A.; Stella, V. J., Pharmaceutical applications of cyclodextrins. 2. In vivo drug delivery. *J. Pharm. Sci.* **1996,** *85* (11), 1142-1169.

11. Baghel, S.; Cathcart, H.; O'Reilly, N. J., Polymeric amorphous solid dispersions: A review of amorphization, crystallization, stabilization, solid-state characterization, and aqueous solubilization of biopharmaceutical classification system cass II drugs. *J. Pharm. Sci.* **2016,** *105* (9), 2527-2544.

12. Van den Mooter, G., The use of amorphous solid dispersions: A formulation strategy to overcome poor solubility and dissolution rate. *Drug Discov. Today Technol.* **2012,** *9* (2), e79-e85.

13. Purohit, H. S.; Taylor, L. S., Phase behavior of ritonavir amorphous solid dispersions during hydration and dissolution. *Pharm. Res.* **2017,** *34* (12), 2842-2861.

14. Ricarte, R. G.; Li, Z.; Johnson, L. M.; Ting, J. M.; Reineke, T. M.; Bates, F. S.; Hillmyer, M. A.; Lodge, T. P., Direct observation of nanostructures during aqueous dissolution of polymer/drug particles. *Macromolecules* **2017,** *50* (8), 3143-3152.

15. Wais, U.; Jackson, A. W.; He, T.; Zhang, H., Nanoformulation and encapsulation approaches for poorly water-soluble drug nanoparticles. *Nanoscale* **2016,** *8* (4), 1746-1769.

16. Kalepu, S.; Nekkanti, V., Insoluble drug delivery strategies: review of recent advances and business prospects. *Acta. Pharm. Sin. B.* **2015,** *5* (5), 442-453.

17. Chen, H.; Khemtong, C.; Yang, X.; Chang, X.; Gao, J., Nanonization strategies for poorly water-soluble drugs. *Drug. Discov. Today.* **2011,** *16* (7), 354-360.

18. Dizaj, S. M.; Vazifehasl, Z.; Salatin, S.; Adibkia, K.; Javadzadeh, Y., Nanosizing of drugs: Effect on dissolution rate. *Res. Pharm. Sci.* **2015,** *10* (2), 95-108.

19. Chaudhary, A.; Nagaich, U.; Gulati, N.; Sharma, V.; Khosa, R. L. In Enhancement of solubilization and bioavailability of poorly soluble drugs by physical and chemical modifications : A recent review, *J. Adv. Pharm. Educ. Res*. **2012**, pp 32-67.
20. Merisko-Liversidge, E.; Liversidge, G. G.; Cooper, E. R., Nanosizing: a formulation approach for poorly-water-soluble compounds. *Eur. J. Pharm. Sci.* **2003,** *18* (2), 113-20.
21. Ensign, L. M.; Cone, R.; Hanes, J., Oral drug delivery with polymeric nanoparticles: the gastrointestinal mucus barriers. *Adv. Drug. Deliv. Rev.* **2012,** *64* (6), 557-570.
22. Jog, R.; Burgess, D. J., Pharmaceutical amorphous nanoparticles. *J. Pharm. Sci.* **2017,** *106* (1), 39-65.
23. Curatolo, W.; Nightingale, J. A.; Herbig, S. M., Utility of hydroxypropylmethylcellulose acetate succinate (HPMCAS) for initiation and maintenance of drug supersaturation in the GI milieu. *Pharm. Res.* **2009,** *26* (6), 1419-1431.
24. Tachibana, T.; Nakamura, A., A methode for preparing an aqueous colloidal dispersion of organic materials by using water-soluble polymers: Dispersion of beta-carotene by polyvinylpyrrolidone. *Kolloid-Z.Z. Polym.* **1965,** *203* (2), 130-133.
25. Alonzo, D. E.; Gao, Y.; Zhou, D.; Mo, H.; Zhang, G. G. Z.; Taylor, L. S., Dissolution and precipitation behavior of amorphous solid dispersions. *J. Pharm. Sci.* **2011,** *100* (8), 3316-3331.
26. Shudo, J.; Pongpeerapat, A.; Wanawongthai, C.; Moribe, K.; Yamamoto, K., In vivo assessment of oral administration of probucol nanoparticles in rats. *Biol. Pharm. Bull.* **2008,** *31* (2), 321-325.
27. Janssens, S.; De Zeure, A.; Paudel, A.; Van Humbeeck, J.; Rombaut, P.; Van den Mooter, G., Influence of preparation methods on solid state supersaturation of amorphous solid dispersions: a case study with itraconazole and Eudragit E100. *Pharm. Res.* **2010,** *27* (5), 775-785.
28. Shi, C.; Li, L.; Zhang, G. G. Z.; Borchardt, T. B., Direct visualization of drug-polymer phase separation in ritonavir-copovidone amorphous solid dispersions using in situ synchrotron X-ray fluorescence imaging of thin films. *Mol. Pharmaceutics.* **2019,** *16* (11), 4751-4754.
29. Chen, H.; Pui, Y.; Liu, C.; Chen, Z.; Su, C. C.; Hageman, M.; Hussain, M.; Haskell, R.; Stefanski, K.; Foster, K.; Gudmundsson, O.; Qian, F., Moisture-induced amorphous phase separation of amorphous solid dispersions: molecular mechanism, microstructure, and Its impact on dissolution performance. *J. Pharm. Sci.* **2018,** *107* (1), 317-326.
30. Purohit, H. S.; Taylor, L. S., Phase separation kinetics in amorphous solid dispersions upon exposure to water. *Mol. Pharmaceutics.* **2015,** *12* (5), 1623-1635.
31. Rumondor, A. C.; Taylor, L. S., Effect of polymer hygroscopicity on the phase behavior of amorphous solid dispersions in the presence of moisture. *Mol. Pharmaceutics.* **2010,** *7* (2), 477-490.
32. Li, N.; Taylor, L. S., Microstructure formation for improved dissolution performance of lopinavir amorphous solid dispersions. *Mol. Pharmaceutics.* **2019,** *16* (4), 1751-1765.
33. Wu, L.; Zhang, J.; Watanabe, W., Physical and chemical stability of drug nanoparticles. *Adv. Drug Deliv Rev.* **2011,** *63* (6), 456-469.
34. Pongpeerapat, A.; Wanawongthai, C.; Tozuka, Y.; Moribe, K.; Yamamoto, K., Formation mechanism of colloidal nanoparticles obtained from probucol/PVP/SDS ternary ground mixture. *Int. J. Pharm.* **2008,** *352* (1-2), 309-316.
35. Sievens-Figueroa, L.; Bhakay, A.; Jerez-Rozo, J. I.; Pandya, N.; Romanach, R. J.; Michniak-Kohn, B.; Iqbal, Z.; Bilgili, E.; Dave, R. N., Preparation and characterization of hydroxypropyl methyl cellulose films containing stable BCS Class II drug nanoparticles for

pharmaceutical applications. *Int. J. Pharm.* **2012,** *423* (2), 496-508.
36. Friesen, D. T.; Shanker, R.; Crew, M.; Smithey, D. T.; Curatolo, W. J.; Nightingale, J. A., Hydroxypropyl methylcellulose acetate succinate-based spray-dried dispersions: an overview. *Mol Pharmaceut* **2008,** *5* (6), 1003-1019.
37. Moribe, K.; Ogino, A.; Kumamoto, T.; Ishikawa, T.; Limwikrant, W.; Higashi, K.; Yamamoto, K., Mechanism of nanoparticle formation from ternary coground phenytoin and its derivatives. *J. Pharm. Sci.* **2012,** *101* (9), 3413-3424.
38. Kipp, J. E., The role of solid nanoparticle technology in the parenteral delivery of poorly water-soluble drugs. *Int. J. Pharm.* **2004,** *284* (1-2), 109-122.
39. Ilevbare, G. A.; Liu, H. Y.; Pereira, J.; Edgar, K. J.; Taylor, L. S., Influence of additives on the properties of nanodroplets formed in highly supersaturated aqueous solutions of ritonavir. *Mol. Pharmaceutics.* **2013,** *10* (9), 3392-3403.
40. Ambhore, N. P.; Dandagi, P. M.; Gadad, A. P., Formulation and comparative evaluation of HPMC and water soluble chitosan-based sparfloxacin nanosuspension for ophthalmic delivery. *Drug. Deliv. Transl. Res.* **2016,** *6* (1), 48-56.
41. Kawakami, K.; Ohba, C., Crystallization of probucol from solution and the glassy state. *Int. J. Pharm.* **2017,** *517* (1-2), 322-328.
42. Bunaciu, A. A.; Udristioiu, E. G.; Aboul-Enein, H. Y., X-ray diffraction: instrumentation and applications. *Crit. Rev. Anal. Chem.* **2015,** *45* (4), 289-299.
43. Zhao, Z.; Katai, H.; Higashi, K.; Ueda, K.; Kawakami, K.; Moribe, K., Cryo-TEM and AFM observation of the time-dependent evolution of amorphous probucol nanoparticles formed by the aqueous dispersion of ternary solid dispersions. *Mol. Pharmaceutics.* **2019,** *16* (5), 2184-2198.
44. Geppi, M.; Guccione, S.; Mollica, G.; Pignatello, R.; Veracini, C. A., Molecular properties of ibuprofen and its solid dispersions with Eudragit RL100 studied by solid-state nuclear magnetic resonance. *Pharm. Res.* **2005,** *22* (9), 1544-1555.
45. Danaei, M.; Dehghankhold, M.; Ataei, S.; Hasanzadeh Davarani, F.; Javanmard, R.; Dokhani, A.; Khorasani, S.; Mozafari, M. R., Impact of particle size and polydispersity index on the clinical applications of lipidic nanocarrier systems. *Pharmaceutics* **2018,** *10* (2), 57.
46. Wang, H.; Sun, Y.; Yang, B.; Li, S., Association between the physical stability of flurbiprofen suspension and the interaction of HPMC/SDS. *Asian J. Pharm. Sci.* **2018,** *13* (1), 63-71.
47. Egami, K.; Higashi, K.; Yamamoto, K.; Moribe, K., Crystallization of probucol in nanoparticles revealed by AFM analysis in aqueous solution. *Mol. Pharmaceutics.* **2015,** *12* (8), 2972-2980.
48. Yonashiro, H.; Higashi, K.; Morikawa, C.; Ueda, K.; Itoh, T.; Ito, M.; Masu, H.; Noguchi, S.; Moribe, K., Morphological and physicochemical evaluation of two distinct glibenclamide/hypromellose amorphous nanoparticles prepared by the antisolvent method. *Mol. Pharmaceutics.* **2018,** *15* (4), 1587-1597.
49. Zhang, C.; Guo, Y. L.; Priestley, R. D., Glass transition temperature of polymer nanoparticles under soft and hard confinement. *Macromolecules* **2011,** *44* (10), 4001-4006.
50. Perez-de-Eulate, N. G.; Di Lisio, V.; Cangialosi, D., Glass transition and molecular dynamics in polystyrene nanospheres by fast scanning calorimetry. *Acs Macro Lett* **2017,** *6* (8), 859-863.
51. Kuntsche, J.; Horst, J. C.; Bunjes, H., Cryogenic transmission electron microscopy (cryo-TEM) for studying the morphology of colloidal drug delivery systems. *Int. J. Pharm.* **2011,** *417* (1-2), 120-37.
52. Li, N.; Taylor, L. S., Nanoscale infrared, thermal, and mechanical characterization of

telaprevir-polymer miscibility in amorphous solid dispersions prepared by solvent evaporation. *Mol. Pharmaceutics.* **2016,** *13* (3), 1123-1136.

53. Maghsoodi, M.; Nokhodchi, A., Agglomeration of celecoxib by quasi emulsion solvent diffusion method: Effect of stabilizer. *Adv. Pharm. Bull.* **2016,** *6* (4), 607-616.

54. Mullin, J. W., 6-Crystal growth. In *Crystallization (Fourth Edition)*, Mullin, J. W., Ed. Butterworth-Heinemann: Oxford, 2001; pp 216-288.

55. Konno, H.; Taylor, L. S., Ability of different polymers to inhibit the crystallization of amorphous felodipine in the presence of moisture. *Pharm. Res.* **2008,** *25* (4), 969-978.

56. Ting, J. M.; Porter, W. W., 3rd; Mecca, J. M.; Bates, F. S.; Reineke, T. M., Advances in Polymer Design for Enhancing Oral Drug Solubility and Delivery. *Bioconjug. Chem.* **2018,** *29* (4), 939-952.

57. Cheow, W. S.; Kiew, T. Y.; Yang, Y.; Hadinoto, K., Amorphization strategy affects the stability and supersaturation profile of amorphous drug nanoparticles. *Mol. Pharmaceutics.* **2014,** *11* (5), 1611-1620.

58. Dave, R. H.; Patel, A. D.; Donahue, E.; Patel, H. H., To evaluate the effect of addition of an anionic surfactant on solid dispersion using model drug indomethacin. *Drug Dev. Ind. Pharm.* **2012,** *38* (8), 930-939.

59. Flory, P. J., Thermodynamics of high polymer solutions. *J. Chem. Phys.* **1942,** *10* (1), 51-61.

60. Huggins, M. L., Thermodynamic properties of solutions of long-chain compounds. *Ann. N. Y. Acad. Sci.* **1942,** *43* (1), 1-32.

61. Marsac, P. J.; Shamblin, S. L.; Taylor, L. S., Theoretical and practical approaches for prediction of drug-polymer miscibility and solubility. *Pharm. Res.* **2006,** *23* (10), 2417-2426.

62. Marsac, P. J.; Li, T.; Taylor, L. S., Estimation of drug-polymer miscibility and solubility in amorphous solid dispersions using experimentally determined interaction parameters. *Pharm. Res.* **2009,** *26* (1), 139-151.

LIST OF PUBLICATIONS

This thesis is based on the following publications:

Zhao, Z.; Katai, H.; Higashi, K.; Ueda, K.; Kawakami, K.; Moribe, K., Cryo-TEM and AFM observation of the time-dependent evolution of amorphous probucol nanoparticles formed by the aqueous dispersion of ternary solid dispersions. *Mol. Pharmaceutics.* **2019,** *16* (5), 2184-2198.

THESIS COMMITTEE

This thesis, conducted for the Degree of Doctral of Philosophy (Pharmaceutical Sciences) was examined by the following committee, authorized by the Graduate School of Pharmaceutical Sciences, Chiba University, Japan.

Professor Hidetaka Akita, Ph.D. Chairman

(Graduate School of Pharmaceutical Sciences, Chiba University)

Professor Noritaka Nishida, Ph.D.

(Graduate School of Pharmaceutical Sciences, Chiba University)

Professor Yukihiro Ikeda, Ph.D.

(Graduate School of Pharmaceutical Sciences, Chiba University)